Accelerated signal propagation speed in human neocortical dendrites

Short title: Signal propagation in human microcircuits

Gáspár Oláh[1,5†], Rajmund Lákovics[1†], Sapir Shapira[2†], Yoni Leibner[2], Attila Szűcs[3], Éva Adrienn Csajbók[1], Pál Barzó[4], Gábor Molnár[1*], Idan Segev[2*], Gábor Tamás[1*]

Affiliations

[1] ELKH-SZTE Research Group for Cortical Microcircuits, Department of Physiology, Anatomy and Neuroscience, University of Szeged, Szeged, Hungary

[2] Edmond and Lily Safra center for Brain Sciences, The Hebrew University of Jerusalem, Jerusalem, Israel

[3] Department of Physiology and Neurobiology, Institute of Biology, Eötvös Loránd University, Budapest, Hungary

[4] Department of Neurosurgery, University of Szeged, Szeged, Hungary

[5] Current affiliation: Laboratory of Cellular Neurophysiology, ELKH, Institute of Experimental Medicine, Budapest, Hungary

[†]: These authors contributed equally.

*: Equal contribution of senior authors, correspondence: gtamas@bio.u-szeged.hu

Abstract

Human-specific cognitive abilities depend on information processing in the cerebral cortex, where the neurons are significantly larger and their processes longer and sparser compared to rodents. We found that, in synaptically connected layer 2/3 pyramidal cells (L2/3 PCs), the delay in signal propagation from soma to soma is similar in humans and rodents. To compensate for the longer processes of neurons, membrane potential changes in human axons and/or dendrites must propagate faster. Dual somato-dendritic and somato-axonal patch recordings show that the propagation speed of action potentials (APs) is similar in human and rat axons, but the forward propagation of excitatory postsynaptic potentials (EPSPs) and the backward propagation of APs are 26 and 47% faster in human dendrites, respectively. Accurate biophysical models of human and rat L2/3 PCs, combined with pharmacological manipulations of membrane properties, have shown that various factors enhance EPSP propagation in humans; the key factor is the large conductance load imposed by the large basal dendritic tree in humans, the key factor responsible for the accelerated signal propagation in human cortical dendrites. Larger dendritic diameter in humans as well as differences in cable and ion channel properties, also contribute to the enhancement of signal propagation in human L2/3 dendrites.

Introduction

The human neocortex is thought to be one of the most complex biological structures yet most of our knowledge regarding the properties of individual cortical neurons and their synapses is based on experiments performed in model organisms. Recent findings in human specimens indicated the emergence of new cell types in the human neocortex(Ballesteros Yáñez et al., 2005; Berg et al., 2021; Boldog et al., 2018; Deitcher et al., 2017; Oberheim et al., 2009) and species related differences in transmitter release probability (Molnár et al., 2016), regenerative dendritic events (Beaulieu-Laroche et al., 2018, 2021; Gidon et al., 2020), ion channel composition of the dendrites (Kalmbach et al., 2018), temporal dynamics of synaptic potentiation (Verhoog et al., 2013) and activity patterns of the microcircuits (Komlósi et al., 2012; Molnár et al., 2008; Szegedi et al., 2016). Pioneering experiments indicate that human dendrites could evolve in ways favoring mechanisms not yet found in other species (Beaulieu-Laroche et al., 2018; Gidon et al., 2020) and might contribute to the apparent efficacy of human cognitive performance (Goriounova et al., 2018). Functional differences are accompanied by a divergence in morphological features, ranging from general alterations in the thickness of cortical layers to increasing complexity in anatomical properties of classical cell types (Deitcher et al., 2017; Mohan et al., 2015). Human pyramidal cells with larger and more extensively branching dendritic trees have an opportunity to receive a higher number of synaptic inputs (Benavides-Piccione et al., 2020; Loomba et al., 2022). This, when combined with the increased morphological complexity, endows human cortical neurons with enhanced computational and encoding capabilities (Beaulieu-Laroche et al., 2021; Deitcher et al., 2017).

However, the increase in size of dendrites and axons might come with a cost of longer signal propagation times of both synaptic potentials in dendrites (larger dendritic delay) as well as action potentials in axons (axonal delay). This will slow down information processing, both within individual cortical neurons as well as in respective cortical circuits(Buzsáki et al., 2013; Vetter et al., 2001). Indeed, transferring large amounts of information within and between brain regions in a short amount of time, and the capability of the neuronal circuit to respond sufficiently fast to its environment, is an important evolutionary function of neuronal networks(Buzsáki et al., 2013; Laughlin & Sejnowski, 2003). Increased cell-to-cell delay will also affect plasticity/learning processes that depend on the timing between the pre- and the post-synaptic action potentials, e.g., the spike-timing-dependent plasticity (STDP) mechanism. It was therefore suggested that certain scaling morphological rules must be applied so that animals with larger brains can still function adequately in their environment (West et al., 1997). Is that the case for cortical neurons in human?

We set out in this study to directly measure the speed of signal propagation in both dendrites and axons of individual human and rat L2/3 pyramidal cells and applied experiments-based models to identify cellular and subcellular properties involved in controlling neuron-to-neuron propagation delays. Our integrative experimental and modeling study provides insights into the scaling rules that enable to preserve information processing speed albeit the much larger neurons in the human cortex.

Results

Signal propagation paths and delays in human and rat pyramid to pyramid connections

We followed recent results indicating differences in the density and size of human and mouse supragranular pyramidal cells (PCs) (Berg et al., 2021) in a human-rat setting. As expected, measurements on 3D reconstructions based on randomly selected, electrophysiologically recorded and biocytin filled human (n = 30) and rat (n = 30) L2/3 cortical pyramidal cells (Fig. S1A) show significant differences in the horizontal (463.17 ± 119.48 vs. 324.79 ± 80.58 µm, *t* test: P = 1.687 × 10^{-6}) and vertical extensions (542.58 ± 146.89 vs. 409.99 ± 102.69 µm, *t* test: P = 0.00013), and in the total dendritic (9054.94 ± 3699.71 vs. 5162.68 ± 1237.71 µm, *t* test: P = 7.203 × 10^{-7}) and apical dendritic length (4349.76 ± 1638.39 vs. 2592.15 ± 818.26 µm, *t* test: P = 1.638 × 10^{-6}, Fig. S1B,C).

To examine the temporal aspects of information propagation in excitatory microcircuits, we performed simultaneous whole cell patch clamp recordings in synaptically connected L2/3 PCs from acute neocortical slices from rat and human tissues (Fig. 1). Excitatory postsynaptic potentials (EPSPs) were measured in response to single action potentials (AP) in presynaptic cells (Fig. 1B). Synaptic latency was calculated as the time difference between the peak of the presynaptic AP and the onset point of the postsynaptic EPSP (see Fig 1B and Methods). We did not find significant differences in synaptic latencies between human and rat PC-to-PC connections (rat: 1.126 ± 0.378 ms, rat: n = 19, human: 1.111 ± 0.306 ms, n = 17, Mann-Whitney test: P = 0.949). Both pre- and postsynaptic PCs were filled with biocytin during recordings allowing for post hoc identification of close appositions between presynaptic axons and postsynaptic dendrites (Frick et al., 2008) (Fig. 1A). We measured the shortest axonal path lengths linking the presynaptic soma to close appositions on the postsynaptic dendrite (rat: 168.267 ± 49.59 µm, human: 272.22 ± 73.14 µm) and the shortest dendritic path lengths from close appositions found exclusively on dendritic spine heads to the postsynaptic soma (rat: 84.9 ± 18.301 µm, human: 129.48 ± 40.005 µm) in a subset of recordings (rat: n = 6, human: n = 5). Consequently, we found that the minimal intersomatic distance (the sum of the shortest axonal and dendritic paths) in each synaptically connected PC-to-PC pair was significantly smaller in rats compared to humans (rat: 259.7 ± 58.8 µm, human: 402.12 ± 74.757 µm, Mann-Whitney test: P = 0.009, Fig. 1D). We did not find significant difference in these paired recordings in synaptic latency (rat: 1.09 ± 0.375 ms, n = 6 from n = 6 rats; human: 1.102 ± 0.408 ms, n = 5 from n = 5 patients; Mann-Whitney test: P = 0.931, Fig. 1C, darker dots). Given that similar synaptic latencies accompany different lengths for signal propagation in the two species, membrane potentials (APs and/or EPSPs) are likely to propagate faster in human PC-to-PC connections.

Direct measurements of signal propagation in PC dendrites and axons

Compensation of longer axonal and dendritic paths must be explained by higher velocity of signal propagation along axons and/or dendrites. We therefore asked whether interspecies differences can be found in axonal and/or dendritic signal propagation in L2/3 PCs.

First, we investigated whether we could find dissimilarities between the two species in the speed of signal propagation along axons of PCs. We whole cell recorded the soma and a distal axon simultaneously, positioning the axonal recording electrode on one of the blebs formed at the cut ends of axons during slice preparation. Somatic current injections were used to trigger APs and the time between somatic and the axonal AP was measured (Fig. 2A, Fig S2C). We captured two-photon images during electrophysiological recording and measured the length of the axonal path from the somatic to the axonal electrode on image z-stacks. The dataset was restricted to recordings that matched the distances from the soma to axo-dendritic close appositions determined above along the axon of synaptically coupled PC-to-PC connections (rat: n = 8, 268.203 ± 76.149 µm vs. human: n = 9, 281.507 ± 125.681 µm, two sample *t* test: P = 0.799, Fig. 2F). The latency between the soma and the axon bleb of the propagating AP peaks was not significantly different between the species

(rat: n = 8, 0.333 ± 0.211 ms vs. human: n = 9, 0.327 ± 0.123 ms, two sample *t* test: P = 0.945). The axonal speed of AP propagation was calculated for each cell from the time required from soma to recording site. We found no significant difference in the propagation speed of APs in the axons of rats and humans (rat: n = 8, 0.848 ± 0.291 m/s vs. human: n = 9, 0.851 ± 0.387 m/s, two sample *t*-test: P = 0.282, Fig. 2F). Our axonal recordings suggest that there is no significant difference between the two species over the range of distances we investigated, so the lower latencies in the paired recordings may be due to dendritic differences.

We next sought to test rat and human dendritic signal propagation velocity using simultaneous whole cell patch clamp recordings with electrodes placed on the somata and dendritic shafts of PCs. Distances of somatic and dendritic recording locations (rat: 143.078 ± 72.422 µm, n = 46; vs. human: 153.446 ± 57.698 µm, n = 62, Mann-Whitney test: P = 0.175, Fig. 2B) were chosen to be similar in the two species and in range of soma-to-dendrite distances of axo-dendritic close appositions determined above for synaptically coupled PC-to-PC connections. In the first set of experiments, we injected suprathreshold current through the somatic electrode and measured the time difference between the evoked AP peak at the soma and the respective backpropagating AP peak in the dendritic electrode (Fig. 2E and F). We found significant difference in the signal propagation time between rat and human PCs (rat: 0.672 ± 0.334 ms, n = 46; vs. human: 0.495 ± 0.229 ms, n = 62, Mann-Whitney test: P = 0.005, Fig. 2F). The AP propagation speed was calculated for each cell from the time difference between the somatic and dendritic APs divided by the distance between the two points. We found that the propagation speed was, on average, ~1.47-fold faster in human (rat: 0.233 ± 0.095 m/s vs. human: 0.344 ± 0.139 m/s, Mann-Whitney test: P = 6.369×10^{-6}, Fig. 2F, Fig S2B). In a second set of experiments, using the same dual recording configuration, we tested orthodromic or forward propagating signal propagation velocity by injecting short-duration current ramps to simulate EPSP (sEPSP) signals in the dendrites and recorded the resultant subthreshold voltage response in the soma (Fig. 2C). These experiments were performed in the same PCs where backpropagating AP velocities were also measured (rat: n = 24, human: n = 24). We found that sEPSP propagation speed was, on average, ~1.26-fold faster in human (rat: 0.074 ± 0.018 m/s vs. human: 0.093 ± 0.025 m/s, two sample *t* test: P = 0.004; Fig. 2D, Fig S2D). In addition, we found correlation between forward propagating sEPSP speed and back propagating AP speed (Pearson correlation coefficient, r = 0.396, P = 0.0053, Fig. 2D).

Contribution of ion channels of the dendritic membrane to signal propagation velocity

Hyperpolarization-activated cyclic nucleotide-modulated (HCN) channel densities were shown to be higher in human compared to rat layer 2/3 PCs and were shown to be instrumental in more depolarized resting membrane potentials and in larger sag potentials in response to hyperpolarization in the human (Kalmbach et al., 2018). In addition, modeling predicted that signal delay in dendrites reduces with increased h-conductance (Kalmbach et al., 2018). In line with previous studies, human PCs in our dataset had more depolarized resting membrane potential (rat: -70.49 ± 5.78 mV, human: -64.30 ± 7.28 mV, Mann-Whitney U test: P = 7.37×10^{-6}, Fig. S3A) but the average somatic input resistance were not significantly different in the two species (rat: 59.56 ± 21.86 MΩ, n = 46, human: 71.375 ± 65.485 MΩ, n = 62, Mann-Whitney test: P = 0.347, Fig. S3A).

Based on the correlation found between forward-propagating sEPSP speed and back-propagating AP speed, we performed pharmacological experiments on bAPs (since it is technically less challenging to evoke) to uncover potential contributors to increased dendritic speeds in humans. To test the contribution of h-channels to the elevated signal propagation speed in human dendrites, we performed pharmacological experiments with 20 µM ZD7288, a specific blocker of h-channels. Significant hyperpolarization of the resting membrane potential was observed in the human cells

but not in the rat neurons (Fig. S3B) and significantly increased input resistance accompanied drug application in both human and rat neurons (Fig. S3C). Drug administration did not significantly decrease bAP propagation speed in rat PCs (control: 0.163 ± 0.054 m/s, ZD7288: 0.149 ± 0.057 m/s, n = 9, two-way ANOVA with repeated measures and and Tukey HSD (Honestly Significant Difference) post-hoc comparison: P = 0.9, Fig. 3A, Fig S2E) and in human PCs (control: 0.322 ± 0.073 m/s, ZD7288: 0.268 ± 0.066 m/s, n = 8, two-way ANOVA with repeated measures and Tukey HSD post-hoc comparison: P = 0.329, Fig. 3B, Fig S2E). The human dendrites maintained a higher bAP propagation speed in response to h-channel blockage (two-way ANOVA with repeated measures and Tukey HSD post-hoc comparison: P = 0.003). We could not find significant interaction of species and ZD7288 treatment (two-way ANOVA with repeated measures: interaction P=0.358). These results suggest that the species-dependent density difference of HCN channels of pyramidal apical dendrites do not by themselves explain the propagation speed differences between the two species.

Back-propagation of APs is an active process supported by voltage gated ion channels that can initiate regenerative events in the dendrites(Stuart & Sakmann, 1994). To further investigate the influence of voltage gated ion channels we pharmacologically blocked voltage gated Na^+ channels with tetrodotoxin (TTX, 1μM), voltage gated Ca^{2+} channels with cadmium chloride ($CdCl_2$, 200 μM), and NMDA receptors with (2*R*)-amino-5-phosphonovaleric acid (AP5, 20 μM) simultaneously. Since the blockage of voltage gated Na^+ channels prevent the initiation of APs, we kept the soma of the recorded cells in voltage clamp mode and used a prerecorded template as voltage command through a somatically placed electrode (the so called “simulated spike”) and measured the back propagation of the response to the somatic voltage command at a dendritic recording site in current clamp mode. As expected, the amplitude of the bAPs at the dendritic recording site dropped significantly in human and rat cells respectively (Fig. S3D). The speed of back propagation of membrane potential signals in dendrites with blocked regenerative events by the pharmacological cocktail was significantly reduced in rat samples compared to the drug-free control (rat control: 0.199 ± 0.053 m/s, rat TTX/$CdCl_2$/AP5: 0.076 ± 0.03 m/s, two-way ANOVA and Tukey HSD post-hoc comparison: P = 0.024, Fig. 3D, Fig S2F), and was significantly lower in human samples as well (human control: 0.395 ± 0.14 m/s, human TTX/$CdCl_2$/AP5: 0.184 ± 0.061 m/s, two-way ANOVA and Tukey HSD post-hoc comparison: P = 0.001, Fig. 3E, Fig S2F). The human dendrites with blocked action potential generation on average had a higher bAP propagation speed however it was not statistically significant (rat: 0.076 ± 0.03 m/s n = 8, human: 0.184 ± 0.061 m/s n = 8, two-way ANOVA with repeated measures and Tukey HSD post-hoc comparison: P = 0.066). We could not find significant interaction of species and drug treatment (two-way ANOVA with repeated measures, interaction: P=0.142). In summary, in the search for factors contributing to higher signal propagation speeds in human pyramidal dendrites compared to rat pyramidal dendrites, ion channels such as voltage-gated Na^+, Ca^{2+} and NMDA channels and the HCN seem to play a minor role in distinguishing the two species.

Specific membrane capacitance

The specific membrane capacitance (C_m) can influence the time constant of the biological membrane, and it is a key determinant of the propagation of electrical signals. Recent experiments indicated that the C_m of human L2/3 PCs might be significantly lower compared to rodents (Eyal et al., 2016) and modeling studies suggested that the decrease in C_m could lead to increased conduction speed and fewer synapses being able to evoke suprathreshold events in human PCs (Eyal et al., 2016). However, a separate line of experiments could not detect differences in the C_m of L5 PCs between humans and rodents (Beaulieu-Laroche et al., 2018), or L2/3 PCs (Gooch et al., 2022) thus, to test whether C_m is a component in producing elevated signal propagation velocity in human dendrites, we directly measured the C_m values of human and rat PCs by pulling nucleated

patches (Eyal et al., 2016) (Fig. 4A,B). We found no significant difference in the C_m between the human and rat L2/3 PCs (rat: 1.092 ± 0.14 μF/cm^2 n = 20; human: 0.987 ± 0.196 μF/cm^2 n = 19, two-sample *t* test: P = 0.0615, Fig. 4C). The specific membrane capacitance is determined by the dielectric constant of the membrane, and it is inversely proportional with the membrane thickness. We measured the membrane thickness of dendritic structures with transmission electron microscopy both in human and rat samples (Fig. 4D,E) and detected no significant differences between the two species (human: 4.271 ± 0.873 nm, n = 213 from n = 3 patient; rat: 4.122 ± 0.779 nm n = 151 from n = 3 rat, Mann-Whitney test: P = 0.212, Fig. 4E). Based on these experiments it seems that not the specific membrane capacitance is the key determinant of the higher signal propagation speed in human cells.

Effect of dendritic thickness

The relationship between conduction velocity and axon diameter is well known for small myelinated and unmyelinated axons (Waxman & Bennett, 1972). Anatomical features of neuronal dendrites also have a major influence on signal propagation properties (Deitcher et al., 2017; Rall & Rinzel, 1973; Rinzel & Rall, 1974; Vetter et al., 2001), thus, in addition to the soma-dendritic path measurements shown above, we also measured the thickness of dendrites at every 0.5 μm along the path linking the somatic and dendritic electrodes on two-photon image stacks captured during electrophysiological measurements (Fig. 5A-C). We found that the mean diameter of dendrites was thicker in human (2.272 ± 0.584 μm, n = 62) compared to the rat (2.032 ± 0.413 μm, n = 46, two sample *t* test: P = 0.019, Fig. 5D). Moreover, in samples where we acquired both dendrite thickness and bAP signal propagation velocity, we found that the mean dendritic diameter between the recording sites was correlated with the speed of backpropagating APs (Fig. 5E).

Modeling EPSP propagation in dendrites

Detailed compartmental models were utilized to disassemble the effect of various morphological and cable parameters on the latency and velocity of synaptic potential in human and rat L2/3 dendrites. Based on the 3D morphological reconstructions of five human and four rat PCs, we first asked, how dendritic morphological differences *per se* affect signal propagation, assuming that the cable parameters are identical in all cells ($C_m = 1\ \mu F/cm^2$, $R_m = 15{,}000\ \Omega cm^2$, $R_a = 150\ \Omega cm$, Fig. 6). Figure 6A,B shows EPSPs latency and velocity as a function of distance from its dendritic initiation site to the soma. Latency was calculated as the time difference between the peak-times of the local dendritic EPSP and of the resulting somatic EPSP. The dendritic-to-soma latency ranged between 0.1 - 13 ms in rats (red circles) and 0.01 – 25 ms in human (blue circles). The larger maximal latency in human is expected due to the ~2-folds longer apical dendrite in humans L2/3 neurons (Figure 6A). The respective EPSPs velocity was calculated by dividing the path distance to the soma from the dendritic origin of the EPSP by its latency (Figure 6B). EPSP velocity ranged between 0.02 - 0.09 m/s in rat and 0.01 - 0.48 m/s in human (Figure 6B). The exceptionally large differences in the maximal velocity between human and rat is taken in the Discussion.

We next compared signal propagation in rat and human dendrites, focusing on identical range of dendrite-to-soma distances in which the experiments were performed (27 μm – 289 μm, insets in Figure 6A,B). Towards this end, we computed the mean EPSP latency and velocity as a function of distance from the soma, averaged across different branches at a given distance from the soma (Figures 6A, 6B, lower right and upper right insets). For this experimental range of recordings, EPSP velocity ranged between 0.04 - 0.08 m/s in humans versus 0.03 - 0.05 m/s in rats. EPSP latency ranged between 0.1 - 4.7 ms in humans versus 0.4 - 6.5 ms in rats. These findings demonstrate significantly faster EPSP propagation in humans compared to rats (average latency in

humans: 2.45 ± 0.2 ms, n = 5; in rats: 3.3 ± 0.3 ms, n = 4; Mann-Whitney U test: P = 0.03. Average velocity in humans: 0.08 ± 0.005 m/s, n = 5; in rats: 0.05 ± 0.006 m/s, n = 4; Mann-Whitney U test: P = 0.02. See Fig. S10 and Suppl. Table 2).

A possible reason for the smaller latency and larger velocity of EPSPs in human apical dendrites is that they have larger diameter (Figs. 5D and Fig. 6C see also refs. Agmon-Snir & Segev, 1993; Jack et al., 1975). Theory shows that, for an infinitely long passive cylindrical cable, the velocity of passive signals is not constant. It is fast near their site of origin, converging to a value of $2\lambda/\tau$ away from their initiation site (Agmon-Snir & Segev, 1993; Jack et al., 1975) (λ is the cables' space constant and τ is its membrane time constant). This means that the latency and velocity of passive signals, when normalized in units of λ/τ, are identical for cylindrical cables with different diameters. This is due to the fact that differences in cable diameter are taken into account when normalizing the physical distance, x, by λ (which is $\propto \sqrt{d}$, where d is the cable diameter). Hence, if the larger diameter in human dendrites is a key contributor to the enhanced signal velocity in these cells, we expect that the EPSP latency and velocity will converge on similar curves for all cells (rat and human alike) after normalizing the distance in units of λ, and time in units of τ. However, albeit such normalization, the velocity is still larger and the latency is shorter in human (compare insets in Fig. 6D,E to Fig. 6A,B, respectively. In this case, the average latency in humans: 0.16 ± 0.01 τ, n = 5; in rats: 0.22 ± 0.02 τ, n = 4; Mann-Whitney U test: P = 0.02. The average velocity in humans: 2.55 ± 0.11 λ/τ, n=5; in rats: 1.73 ± 0.29 λ/τ, n = 4; Mann-Whitney U test: P = 0.02).

To summarize: Scaling dendritic distance in units of λ and time in units of τ did not eliminate the statistically significant differences in EPSP latency and velocity between humans and rats. This raises the question: what factor enhances EPSP propagation speed in human dendrites?

One possibility is that differences in boundary conditions for EPSPs travelling from the dendrites towards the soma might explain the enhanced signal propagation in human. Boundary conditions are known to affect the steepness of voltage attenuation along the dendrites (Rall & Rinzel, 1973; Rinzel & Rall, 1974). But do differences in the boundary condition ("the impedance load") at the soma affect the speed of EPSPs propagating when travelling from the apical tree towards the soma? Notably, the basal tree in human L2/3 PCs is substantially larger than that of rat (Fig. 6F and Fig. 8A). Quantifying the total membrane area confirms that the basal tree in human is significantly larger than in rats (in humans: 23,621 ± 7,735 μm^2, n = 5; in rats: 9,127 ± 2,759 μm^2, n = 4; Mann-Whitney U test: P = 0.02, see Fig. S11). Consequently, a larger impedance load (larger "sink") is expected at the soma in human L2/3 neurons.

To examine the impact of impedance load, we computationally substituted the basal tree of human neurons with the basal tree of rat and *vice versa* (creating "hybrid cells"). This substitution diminished the inter-species differences in latency and velocity (both in the original units and after normalizing the distance and time in units of λ and τ, respectively). Examples of these "hybrid cells" are shown in Fig. 6G,H. In these cases, the basal trees of the 5 modeled human neurons (blue dots) and the basal tree of "Rat1", "Rat2" and "Rat3" (red dots) were all replaced with the basal tree of "Rat4" neuron. This resulted in a significant reduction in EPSP velocity in the human neurons, diminishing the differences in signal latency/velocity between humans and rats (average latency in humans: 3.42 ± 0.5 ms or 0.23 ± 0.03 in units of τ, n = 5; in rats: 3.2 ± 0.2 ms, 0.21 ± 0.01 in units of τ, n = 4; Mann-Whitney U test: P = 0.7 for both ms and τ units. Average velocity in humans: 0.06 ± 0.005 m/s or 1.86 ± 0.1 λ/τ, n = 5; in rats: 0.05 ± 0.005 m/s or 1.8 ± 0.1 λ/τ, n = 4; Mann-Whitney U test: P = 0.73 for m/s units and P = 0.66 for λ/τ units. See Fig. S10 and Suppl. Table 3). Repeating this procedure for all modeled PCs, but now the basal of any given cell (of both human and rat) was replaced, one-by-one, by the basal tree of all other cells. Again, this confirmed

that the significant difference in EPSPs latency between humans and rats consistently diminished and became insignificant in the "hybrid cell" manipulations. More specifically, human basal trees on rat cells accelerate the EPSPs, whereas rat basal trees on human neurons decelerate the EPSPs (Fig S6).

To further demonstrate the effect of switching the basal tree between human and rat neurons ("hybrid cells") on the EPSPs' velocity and latency, we depict in Figure 6I the case where the basal tree of "Human1" PC was replaced with the basal tree of "Rat4" (top left) and *vice versa* (lower right). The result (the "latency-gram" of the EPSPs) is depicted in color-code, showing deceleration in the apical tree of the human cell (top left) and acceleration in the rat's apical tree (lower right) due to these manipulations. Exemplar somatic EPSPs originated at ~282 μm from the soma in the original cells (black line) and in the respective "hybrid case" (dashed lines) are shown at top right. The deceleration in the case of a human cell with a rat basal tree is shown on the left and the acceleration in the case of a rat cell with a human basal tree is shown on the right. The explanation for the surprising large impact of the impedance load of the basal tree on signal propagation in the apical tree is elaborated in the Discussion.

In addition to morphological features influencing EPSP latency and velocity, the three key passive parameters - specific membrane resistivity (R_m), capacitance (C_m) and axial resistivity (R_a) - affect signal propagation properties in dendrites by altering the cables' space constant (λ) and membrane time constant (τ). These changes can either enhance or compensate for the increased velocity of signal propagation of human cells, depending on the specific values of these parameters. Thus, we next examined to what extent the cable parameters of the individual PCs studied here influence signal propagation in their respective dendrites. To address this, we fitted the cable parameters for each of the 9 reconstructed PCs individually, based on double-electrodes recordings (soma and dendrite) for each cell. Figure 7A shows an exemplar reconstructed human L2/3 PC (Human5) with the locations of the two recording/stimulating electrodes used for this cell. Figure 7B top (D-S: dendrite-to-soma direction) shows the case where the step current was injected at the dendrite (cyan). The resultant voltage response is depicted in cyan in the trace below; the model fit is superimposed in dark blue. The opposite (S-to-D) direction is depicted by the next three traces below. This fit enabled a direct estimate of the cable parameters per cell (Table 1). We found that R_m is larger in humans and C_m is smaller in humans (Table 1). Yet the membrane time constant ($\tau = R_m * C_m$) is statistically similar in the two species (Table 2 and see Fig. S12).

Figure 7C-F extends the simulations using the fitted (rather than uniform) cable parameters for each cell (Fig. 6). Compared to the uniform case, the differences in EPSP latency and propagation velocity between and within the two species are slightly enhanced (compare Fig. 7C,D to Fig. 6A,B). For the per-cell fit, the latency ranges between 0.1 - 11 ms for rats (red) and 0.1 – 28 ms for humans (Fig 7C); the velocity ranges between 0.02 - 0.085 m/s for rats (red) and 0.02 – 0.75 m/s for humans (Fig 7D). After normalizing the distance by the space and time constants calculated per cell, the differences in both latency (Fig. 7E) and velocity (Fig. 7F) among individual cells is larger compared with the uniform case (Figure 6D,E). Importantly, despite this increased variance within species, the differences between humans and rats remain statistically significant, both with and without normalization (average latency in humans: 2.3 ± 0.4 ms, or 0.19 ± 0.03 τ, n = 5; in rats: 3.2 ± 0.6 ms or 0.27 ± 0.05 τ, n = 4; Mann-Whitney U test: P = 0.03 for both ms and τ units. Average velocity in humans: 0.085 ± 0.009 m/s or 2.5 ± 0.4 λ/τ, n = 5; in rats: 0.05 ± 0.0085 m/s or 1.7 ± 0.3 λ/τ, n = 4; Mann-Whitney U test: P = 0.03 for m/s and P = 0.02 for λ/τ units. See Fig. S10 and Table 2).

Next, we applied our "hybrid cells" method (as in Fig. 6 G-I). As a result, the inter-species differences were diminished (average latency in humans: 2.3 ± 0.4 ms, 0.19 ± 0.03 τ, n = 5; in rats: 3.2 ± 0.6 ms, 0.27 ± 0.05 τ, n = 4; Mann-Whitney U test: P = 0.9 for ms units and P = 1.0 τ units. Average velocity for human: 0.08 ± 0.02 m/s, 2.39 ± 0.2 λ/τ, n = 5; rat: 0.05 ± 0.005 m/s, 1.7 ± 0.4 λ/τ n = 4; Mann-Whitney U test: P = 0.2 for m/s and P = 0.8 for λ/τ units. See Fig. S8, Fig. S10 and Suppl. Table 4).

To rank the impact of the various factors affecting EPSP propagation latency in human and rat neurons, we conducted a comprehensive statistical analysis using two complementary approaches: the generalized linear model (GLM) (Kiebel & Holmes, 2007) as well as SHAP (SHapley Additive exPlanations) (Lundberg & Lee, 2017) based on fitting Gradient Tree Boosting model (Friedman, 2002). We began by fitting a GLM without interaction terms among the factors affecting EPSP latency (Suppl. Table 5). This enables us to quantify the primary individual factors affecting EPSP propagation. Our analysis revealed the following ranking order: 1) physical distance of synapses from soma had the strongest effect; 2) species differences; 3) conductance load, as demonstrated by our "hybrid cells" manipulation; 4) radii of the apical dendrite, affecting the cables' space constant, λ; and 5) the specific cable parameters, as revealed when using per-cell fitted parameters versus uniform cable parameters, was minimal. We next performed GLM analysis with interaction terms showing that, as expected, there are significant interactions between the factors affecting EPSP latency (Suppl. Table 6). To further validate the above ranking while incorporating the interactions between the various factors affecting EPSP latency, we performed a SHAP analysis. Notably, even with interactions included, the ranking of the factors affecting signal propagation are aligned with the results from the analysis based on the GLM without interaction terms (see Fig S13).

We summarize this section by noting that our theoretical efforts enabled the dissection of morphological and electrical parameters that affect differences in EPSPs velocity and latency in human versus rat L2/3 PCs' dendrites. We first assumed uniform cable properties for all cells modeled (Fig. 6), showing that the key parameter affecting the enhanced velocity in human neurons is the large increase in conductance load (sink) imposed by the extended basal tree in human PCs. The larger diameter of the apical dendrite in human also contributes, but to a lesser degree, to this effect. Finally, differences in passive cable properties also slightly favor faster signal propagation in humans. Indeed, when the basal tree of human PCs modeled (now with cable parameters fitted per cell) was replaced by the basal tree of rat PCs (and *vice versa*), the interspecies differences diminished – emphasizing again the key impact on signal propagation velocity of the large conductance load at the soma of human L2/3 PCs resulting from the larger basal tree in human PCs (Figs. 7 and 8).

Discussion

Emergence of data concerning conserved and divergent features of different mammalian species in the structure and function of the cerebral cortex suggest fundamental similarity across species (DeFelipe, 2011; Galakhova et al., 2022; Herculano-Houzel, 2011) with a subset of specialized features documented in the human cortex. A number of these specialized properties, like the increase in the size of individual neurons detected early by Ramón y Cajal(Cajal, 1899), have far reaching functional consequences and here we identified some compensatory mechanisms which, in turn, are based on additional specialized features. In particular, we studied propagation velocity of both forward (axonal) and backward (dendritic) action potential, as well as of EPSPs in human and rat dendrites. Our experimentally-based models showed that the average membrane time constant of the two species is similar (~11 ms). Yet, EPSPs arising in the apical dendrite at similar distances from the soma have significantly shorter latency in humans. This results primarily from

the larger diameter of the apical trunk in humans, but also from the difference in cable properties between the two species.

Detailed compartmental models of 3D reconstructed and biophysically measured L2/3 PCs of human and rat L2/3 PCs enabled us to systematically explore factors affecting EPSPs propagation velocity and latency in apical dendrites of these two species. Since the diameter of the apical dendrite is larger in human, and assuming that all specific cable parameters were identical, a synapse located in the apical tree at a given physical distance from the soma is electrotonically closer (in units λ) to the soma in human cells. Consequently, the latency of the dendritic-to-soma EPSP latency is expected to be shorter in human apical dendrites. This shorter cable distance of the human synapse (at a given physical distance) has an additional consequence. The velocity of the EPSP peak in dendritic cables is not constant; it is faster near the synapse, converging to a constant value of $2\lambda/\tau$ away from the synapse (see Agmon-Snir & Segev, 1993). Therefore, EPSPs that originated at electrotonically closer synapses to the soma fall on the steeper (faster) phase of their velocity curve, implying a shorter latency to the soma. But we found that the key factor affecting the propagation velocity of EPSPs toward the soma is the degree of conductance load (the boundary condition) at the soma. We show that the significantly larger basal tree in human L2/3 cells implies a larger conductance load there and as shown in Figures 6 and 8, this enhances EPSP propagation velocity and reduces synaptic latency to the soma (see also Agmon-Snir & Segev, 1993). It is important to note that this increased conductance load (increased sink) in human L2/3 neurons (and probably also in other cortical neurons and other neuron types which are larger in human compared to rat) will enhance EPSPs originated also in the basal and not specifically in the apical tree. The intuitive reason for this enhancement is that the large conductance load (the 'leaky end' boundary conditions) more effectively 'steals' the synaptic (axial) current (like water pouring faster into a large pool). The more mathematical intuition is that the large soma (sink) adds fast time constants to the system (see also the related explanation in Fig. 4 in Eyal et al., 2014).

Additional factors that favor accelerated signal propagation in human L2/3 dendrites are differences in respective specific cable parameters between human and rat (Fig. 7). Additional factors that were not fully explored in the present study, such impedance mismatch due to local morphological irregularities at branch points (Fig. S8) and due to dendritic spines might also play a role in affecting signal propagation speed (Manor et al., 1991) (Fig. S4).

Noteworthy here is that we found that the membrane time constant, τ, is similar in L2/3 PCs of rodents and human implying the preservation of coincidence detection capabilities of dendrites in both species. This is important because coincidence detection in dendrites is a fundamental mechanism for a variety of plasticity mechanisms and computational functions such as directional selectivity, sound localization and expansion of the dynamic range of sensory processing (Agmon-Snir et al., 1998; Rall, 1964; Roome & Kuhn, 2018; Wang et al., 2000) and see review in (Hay et al., 2016).

Multifaceted upscaling of properties found in the human microcircuit is usually considered instrumental in functional enrichment. For example, increase in the number of human supragranular pyramidal cell types compared to the mouse (Berg et al., 2021; Deitcher et al., 2017; Mohan et al., 2015) might help in separating multiple tasks of parallel processing in cortical circuits in and the increased range of synaptic strength in pyramidal output contributes to increased saliency of individual excitatory cells followed by efficient network pattern generation in human (Molnár et al., 2016; Szegedi et al., 2016; Verhoog et al., 2013). However, increase in the size and in morphological complexity of individual neurons might not follow a simple bigger is better logic, but instead it is rather a double-edged sword when considering cellular and microcircuit level

function(Dalügge & Remy, 2018; Fişek & Häusser, 2020; London & Häusser, 2005; Mohan et al., 2015; Spruston et al., 2016; Vetter et al., 2001). On one hand, additional dendritic length can receive a higher number and a more diverse set of inputs contributing to circuit complexity (Loomba et al., 2022) and sophistication of dendritic architecture has been reviewed as the site for elaborate subcellular processing(Beaulieu-Laroche et al., 2021; Deitcher et al., 2017; Galakhova et al., 2022; Gidon et al., 2020; Mohan et al., 2015). On the other hand, signals need to propagate along a longer route through dendritic or axonal trees of increased size. Without compensatory mechanisms, textbook knowledge dictates that longer propagation times and altered waveforms of signals associate with elongated neural processes (Agmon-Snir & Segev, 1993; Buzsáki et al., 2013; Jack et al., 1975; Laughlin & Sejnowski, 2003). Our observation that soma-to-soma pyramidal cell synaptic latencies are similar in human and rodent strongly suggest that compensatory mechanisms evolved together with alterations in dendritic structure such as increased thickness of dendritic segments in the human compared to segments equidistant from the soma in the rat. This finding is backed up by earlier experiments showing similar soma-to-soma latencies between presynaptic pyramidal cells and postsynaptic fast spiking interneurons in human and rat (Molnár et al., 2016) and between human and mouse pre-and postsynaptic cells overall in the neocortex (Campagnola et al., 2022). Thus, it appears that signals connecting pyramid-to-pyramid and pyramid-to-interneuron cell pairs have an evolutionally conserved latency and compensation provided by dendritic structure seems precise. Importantly, based on the datasets available, there is no indication of significant over/under-compensation and acceleration/deceleration of soma-to-soma propagation times.

Precision in monosynaptic latencies across species is instrumental in keeping the timeframe relatively stable for circuit plasticity. Research in animal models laid experimental and theoretical foundations and uncovered bewildering multiplicity of mechanisms explaining the induction and maintenance of plasticity in cortical microcircuits (Bliss & Collingridge, 2019; Dan & Poo, 2004; Debanne et al., 2019; Hebb, 1949; Kullmann et al., 2012; Malenka & Bear, 2004; Markram et al., 2012). In contrast, plasticity is understudied in human samples both at the cellular and microcircuit level (Chittajallu et al., 2020; Mansvelder et al., 2019). Spike time dependent plasticity (STDP) is based on the relative timing of pre-and postsynaptic activity (Caporale & Dan, 2008; Feldman, 2012; Markram et al., 1997) and the paramount feature of STDP experiments to date is that minute jitter between pre- and postsynaptic activity results in major changes in synapse strength (Bi & Poo, 1998; Verhoog et al., 2013). Pioneering STDP studies in human neurons showed a wide temporal STDP window with a reversed STDP curve compared to classic results detected in rodent brain (Bi & Poo, 1998; Verhoog et al., 2013). Interestingly, dendritic L-type voltage-gated calcium channels were found important in human STDP rules (Verhoog et al., 2013), yet our results indicate that dendritic bAP speed is equally influenced by calcium channels in human and rat. However, the faster bAP propagation found here in human PCs is compatible with the shifted STDP rule switch (Verhoog et al., 2013) by allowing postsynaptic somatic action potentials to be generated later yet arriving to dendrites at the same time relative to presynaptic spikes. It remains to be established how altered cable properties reported here interact through a dynamic interplay between potentially human specific dendritic ion channel distribution and local dendritic regenerative processes in order to achieve the reversed STDP curve in human (Beaulieu-Laroche et al., 2018, 2021; Dalügge & Remy, 2018; Fişek & Häusser, 2020; Gidon et al., 2020; Kalmbach et al., 2018).

In addition to associative plasticity, precision of synaptic delays is crucial in the generation of circuit oscillations and network synchronization. Although all known patterns of local field potentials and behavioral correlates present in the human cortex can be detected in other mammals (Buzsáki et al., 2013), fast oscillations are thought to be especially important in cognitive performance (Buzsáki, 2015; Klinzing et al., 2019; Ward, 2003). Fast population rhythms in the cerebral cortex in the gamma and high gamma range are based on alternating activation of

monosynaptically coupled and reciprocally connected pyramidal cells and interneurons (Averkin et al., 2016; Buzsáki & Wang, 2012) and similar mechanisms were proposed for some forms of ripple oscillations (Averkin et al., 2016; Komlósi et al., 2012; Molnár et al., 2008). The relatively small axonal distances and accordingly short axonal AP propagation latencies linking locally connected human PCs and or interneurons found here and earlier (Campagnola et al., 2022; Goriounova et al., 2018; Komlósi et al., 2012; Molnár et al., 2008, 2016; Verhoog et al., 2013) are compatible with the frequency range of fast oscillations. Brief loop times during sequential reactivation of a subset of closely located neurons participating in fast human rhythms are helped by subcellular placement of PC-to-PC (and PC-to-fast spiking interneuron Molnár et al., 2008, 2016) synapses on midrange dendritic segments instead of distal branches and by extremely effective glutamatergic synapses on interneurons triggering postsynaptic spikes in response to unitary input from a PC (Molnár et al., 2008, 2016) in addition to accelerated human dendritic signal propagation. Indeed, latencies of monosynaptic spike-to-spike coupling in single cell triggered Hebbian assemblies characteristic to the human cortical circuit are compatible with up to ~200 Hz frequency (Komlósi et al., 2012; Molnár et al., 2008). Phasic and sequential firing of interneurons and PCs was reported in vivo during fast oscillations in humans (Van Quyen et al., 2016) and single cell spiking sequences emerging during human memory formation are replayed during successful memory retrieval (Vaz et al., 2020) similar to results pioneered in the hippocampus of rodents (Nádasdy et al., 1999; Skaggs & McNaughton, 1996; Wilson & McNaughton, 1994). Our results suggest that changes in human dendritic properties contribute to cross species preservation of fast oscillation related cortical function at the local microcircuit level.

Materials and Methods

Experimental Design

Slice preparation

Experiments were conducted according to the guidelines of University of Szeged Animal Care and Use Committee (ref. no. XX/897/2018) and of the University of Szeged Ethical Committee and Regional Human Investigation Review Board (ref. 75/2014). For all human tissue material written consent was given by the patients prior to surgery. Human neocortical slices were sectioned from material that had to be removed to gain access for the surgical treatment of deep-brain target (n = 33 female and n = 29 male, aged 49 ± 19.2 years, from the frontal (n = 21), temporal (n = 20), parietal (n = 20) and occipital (n = 1) cortices). Anesthesia was induced with intravenous midazolam and fentanyl (0.03 mg/kg, 1–2 µg/kg, respectively). A bolus dose of propofol (1–2 mg/kg) was administered intravenously. The patients received 0.5 mg/kg rocuronium to facilitate endotracheal intubation. The trachea was intubated, and the patient was ventilated with O_2/N_2O mixture at a ratio of 1:2. Anesthesia was maintained with sevoflurane at care volume of 1.2–1.5. Following surgical removal, the resected tissue blocks were immediately immersed into a glass container filled with ice-cold solution in the operating theater and transported to the electrophysiology lab. For animal experiments we used the somatosensory cortex of young adults (19–46 days of age, (P) 23.9 ± 4.9) male Wistar rats. Before decapitation animals were anesthetized by inhalation of halothane. 320 µm thick coronal slices were prepared with a vibration blade microtome (Microm HM 650 V; Microm International GmbH, Walldorf, Germany). Slices were cut in ice-cold (4°C) cutting solution (in mM) 75 sucrose, 84 NaCl, 2.5 KCl, 1 NaH_2PO_4, 25 $NaHCO_3$, 0.5 $CaCl_2$, 4 $MgSO_4$, 25 D(+)-glucose, saturated with 95% O_2 and 5% CO_2. The slices were incubated in 36°C for 30 min, subsequently the solution was changed to (in mM) 130 NaCl, 3.5 KCl, 1 NaH_2PO_4, 24 $NaHCO_3$, 1 $CaCl_2$, 3 $MgSO_4$, 10 D(+)-glucose, saturated with 95% O_2 and 5% CO_2, and the slices were kept in it until experimental use. The solution used for recordings had the same composition except that

the concentrations of $CaCl_2$ and $MgSO_4$ were 3 and 1.5 mM unless it is indicated otherwise. The micropipettes (3–5 MΩ) were filled (in mM) 126 K-gluconate, 4 KCl, 4 ATP-Mg, 0.3 GTP-Na_2, 10 HEPES, 10 phosphocreatine, and 8 biocytin (pH 7.25; 300 mOsm).

In vitro electrophysiology

Somatic whole-cell recordings were obtained at ~37°C from simultaneously recorded PC-PC cell pairs visualized by infrared differential interference contrast (DIC) video microscopy at depths 60–160 µm from the surface of the slice (Zeiss Axio Examiner LSM7; Carl Zeiss AG, Oberkochen, Germany), 40× water-immersion objective (1.0 NA; Carl Zeiss AG, Oberkochen, Germany) equipped with Luigs and Neumann Junior micromanipulator system (Luigs and Neumann, Ratingen, Germany) and HEKA EPC 10 patch clamp amplifier (HEKA Elektronik GmbH, Lambrecht, Germany). Signals were digitalized at 15 kHz and analyzed with custom written scripts in Python. Presynaptic cells were stimulated with a brief suprathreshold current paired pulse (800 pA, 2–3 ms, 50-60 ms separation of the two pulses), derived in 10s interval. The postsynaptic cells were recorded in current-clamp recording, holding current was set to keep the cell's membrane potential around −50 mV. The experiments were stopped if the series resistance (Rs) exceeded 25 MΩ or changed more than 20%. For the dendritic recordings 20 µM Alexa 594 was added to the internal solution of the somatic pipette and 20 µM Alexa 488 to the internal solution of the dendritic pipette. The PCs were kept in whole cell configuration at least 10 minutes before the axon bleb or dendritic targeted recording started. Then the microscope switched to 2p mode. The fluorescent dyes of the pipette solution were excited at 850 nm wavelength with a femtosecond pulsing Ti:sapphire laser (Mai Tai DeepSee, Spectra-Physics, Santa Clara, CA). The axon blebs and the dendrites were targeted in 2p mode. After the successful seal formation, the imaging was switched off to reduce the phototoxicity in the sample. All the recordings were carried out in current clamp mode. 800ms long square pulses with elevating amplitude (from -110 to 300 pA) were used to evoke APs. In some experiments the same long square injection protocol was repeated at the dendritic/axonal recording site. For measuring the forward propagation of electrical signals in dendrites, we applied either short artificial EPSC-shaped currents (Connelly et al., 2016) or mostly ramp currents (Markram & Sakmann, 1994) through the dendritic pipette. 10 minutes of recording we applied different drugs or finished the recordings. At the end of the recording, we acquired a 2p Z series from the recorded dendrite. Then the pipettes were carefully withdrawn from the cells. The slices went under chemical fixation for further anatomical investigation. Due to the small diameter of the dendrites of L2/3 neurons, the dendritic pipette access resistance was 92.43 ± 34.29 MΩ with 24.8-196.2 MΩ range (Gidon et al., 2020). We ran a set of computer simulations on our reconstructed neurons (both of human and rat), adding a simulated electrode with variable serial resistance values. We found that, for series resistances ranging from 40-200 MΩ, the effect of the presence of the electrode on the EPSP latencies is negligible (Fig S9.)

The specific membrane capacitance recordings were carried out as described previously (Gentet et al., 2000). Briefly, the L2/3 PCs were whole cell patch clamped, and a gentle suction made during slow withdrawal of the pipette. The nucleus of the cells were pulled out and the voltage clamped at -70 mV. -5mV voltage steps (repeated 100 times) were applied and the capacitive transients were measured. A DIC image of the nucleus were made for calculation of the membrane surface with the following equation:

$$(1)\ A = \frac{(a+b)^2 * \pi}{4}$$

Where a is the shorter diameter of the ellipse and b is the longer one. After the recording the nucleus was blown away and the pipette tip was pushed into a sylgard ball until the GΩ seal formed. The -5 mV voltage steps were applied again to record the residual capacitance of the system. Before the analysis we subtracted the residual capacitance from the transients.

Pharmacological experiments were carried out on PCs during simultaneous somatic and dendritic recordings after 10 minutes of control recording using ACSF with the following drugs: 20 μM 4-(*N*-ethyl-*N*-phenylamino)-1,2 dimethyl-6-(methylamino)pyrimidinium chloride (ZD7288) (Sigma-Aldrich), or 1 μM TTX, 200 μM $CdCl_2$, and 20 μM AP5.

Post hoc anatomical analysis of recorded cell pairs

After electrophysiological recordings, slices were fixed in a fixative containing 4% paraformaldehyde, 15% picric acid, and 1.25% glutaraldehyde in 0.1 M phosphate buffer (PB; pH = 7.4) at 4°C for at least 12 hr. After several washes in 0.1 M PB, slices were cryoprotected in 10% then 20% sucrose solution in 0.1 M PB. Slices were frozen in liquid nitrogen then thawed in PB, embedded in 10% gelatin, and further sectioned into slices of 60 μm in thickness. Sections were incubated in a solution of conjugated avidin-biotin horseradish peroxidase (ABC; 1:100; Vector Labs) in Tris-buffered saline (TBS, pH = 7.4) at 4°C overnight. The enzyme reaction was revealed by 3'3-diaminobenzidine tetrahydrochloride (0.05%) as chromogen and 0.01% H_2O_2 as an oxidant. Sections were post-fixed with 1% OsO_4 in 0.1 M PB. After several washes in distilled water, sections were stained in 1% uranyl acetate, dehydrated in an ascending series of ethanol. Sections were infiltrated with epoxy resin (Durcupan, Sigma-Aldrich) overnight and embedded on glass slices. 3D light microscopic reconstructions were carried out using the Neurolucida system with a 100× objective. The number of putative synaptic contacts were determined by searching for close appositions of presynaptic axon terminals and postsynaptic dendrites under light microscopy. The distance of the contact sites alongside the branches were measured with Neurolucida. The intersomatic distance was calculated from the branch length from the presynaptic soma to the putative synaptic contact alongside the axon, and the length of the dendrite from the contact site to the postsynaptic soma. If there were more than one putative synapse between the cells, we took the shortest intersomatic path distance for that given cell pair.

Electron microscopy

Sample preparations for the electron microscopy were performed as described previously [2,6]. Briefly, digital images of serial EM sections (20 nm thickness) were taken at 64000x magnification with a FEI/Philips CM10 electron microscope equipped with a MegaView G2 camera. The membrane thickness measurements were carried out on digital images with a custom software. Briefly, postsynaptic dendritic structures were identified with the presence of postsynaptic densities (PSD) faced in front of axon terminals filled with vesicles. At least 20 nm away from the PSD, perpendicular lines were used as region interests (ROI). The intensity line profile of each ROI was calculated, and edge detection was carried out on them. The thickness was determined as the distance between the first and last point along the line profile where the gradient magnitude was larger than 50.

Data analysis

The electrophysiological recordings were analysed by custom written python scripts. First the recorded sweeps were exported with HEKA FitMaster to ascii files. The mean synaptic delay in the paired recordings was determined by the averages of the delays between the peak of single presynaptic action potentials and the onsets of the corresponding EPSPs. The onset was determined by the projection of the intersection of two linear fits on the postsynaptic signal (Fedchyshyn & Wang, 2007). The first line was fitted to the baseline 1 ms window from -0.5 to +0.5 ms of the presynaptic AP peak. The second line was fitted on the rising phase of the EPSP (5-30% of the amplitude). The time point of the crossing lines was projected back to the signal and it was used as the onset (Fig. 1B). For the forward propagation dendritic experiments the latency was calculated on an average signal. The onset of the EPSP-like waveform was determined as the onset of EPSPs in the paired recordings.

The bAP latency was measured at the peak of the average signal for each cell (Stuart & Sakmann, 1994). Only the first APs of the sweeps were averaged to avoid activity dependent Na^+ channel inactivation that can cause a putative modulatory effect on the signal propagation speed. For the axon bleb recordings we assumed that the axon initial segment (AIS) of the cells are 35 µm from the axon hillock (Palmer & Stuart, 2006), and the APs propagate forward (to the bleb) and backward (to the soma) at the same speed. For the correction of the AIS we used the following formula:

$$(2)\ vcorr = \frac{l}{t+(ais/l*t)}$$

where *vcorr* is the corrected propagation speed for AIS position, *l* is the axonal distance between the soma and the axon bleb, *t* is the latency between the two measuring point, *ais* is the assumed position of the AIS alongside the axon (35 µm).

Estimating passive parameters of L2/3 pyramidal cells

We constructed detailed passive compartmental and cable models for five L2/3 human neurons and the four rat L2/3 neurons that were both 3D morphologically reconstructed and biophysically characterized. For each modeled neuron, we optimized the values of three key passive parameters: the specific membrane resistivity and capacitance (R_m, C_m) and the specific axial resistivity, R_a, using Neuron 8.0 (Hines et al., 2009) principal axis optimization algorithm (Brent, 1976; Segev et al., 1989). Optimization was achieved by minimizing the difference between experimental voltage response following hyperpolarizing current steps either to the soma or to the apical dendrite (Fig 7A,B) and the model response. When possible, experimental data was averaged over repetitions of the same stimulus.

To account for the surface area of spines, we used the spine correction factor (F) of 1.9 and 1.5 for human and rat PCs, respectively, by multiplying C_m and dividing R_m by F in segments which are at a distance of at least 60 µm from the soma (Eyal et al., 2016; Hunt et al., 2022). In this study we did not attempt to fit the nonlinear effect of I_h of the voltage response of the cells.

As our experimental data contains simultaneous soma-dendritic pair recordings/stimulation, we decided to fit the voltage response in one location (e.g., the soma) for the current injection in the other location (e.g., dendrites). This is a cleaner way compared to the typical case when only one recording/stimulating electrode is available, as the problem of bridge balance at the current input site does not exist in this case. As we have two recording and simulation sites, we also examined how well the model predicts the local voltage response at the injection site (Fig 7B). Analysis and simulation were conducted using Python 3.8 and visualization using matplotlib 3.15 (Hunter, 2007) and seaborn 0.11 (M. Waskom, 2021).

Modeling EPSP propagation delay and velocity

We used the NEURON simulator (Hines et al., 2009) to model the nine 3D reconstructed neurons (Fig. S5). To compute EPSP's propagation latency and velocity, we simulated EPSPs by injecting a brief transient alpha-shaped current, I_α, delivered either to the soma or in various dendritic loci along the modeled apical tree.

$$(3)\ I_\alpha = A\left(1 - e^{\frac{-t}{\tau_0}}\right) - \left(1 - e^{\frac{-t}{\tau_1}}\right)$$

where $A = 1.5$, $\tau_0 = 0.25$ and $\tau_1 = 1ms$, resulting in EPSP peak time, $t_{peak} = 0.5ms$ and peak current of $I_{peak} = 1.4nA$.

Latency of the resultant EPSP was calculated as the difference between the EPSP peak at all dendritic branches and its resulting EPSP at the soma; using a sampling time bin of 0.01ms. Velocity was calculated as the distance of the input site from soma divided by latency between these two points. Each dot in Figures 6 and 7 is the respective value for a specific dendritic segment in a specific branch of a neuron's apical tree. For each measured feature (radius, and velocity), an inset (zoom-in) matching the experimental distance range was added. It shows the average value across dendritic branches with a given distance from the soma, as a function of distance from soma, smoothed with a rolling 10 µm window. For normalizing the path distance of a given dendritic site to the soma in cable units, we calculated the space constant

$$(4)\ \lambda = \sqrt{d\frac{R_m}{4}R_a}$$

for each dendritic segment (where d is the segment's diameter). We then summed up the cable lengths of all segments along the path from the dendritic location to the soma. Time was normalized by the membrane time constant $\tau = R_m * C_m$. Note that, for segments far enough from cable boundary conditions and stimulus location, velocity approximately equals the theoretical value of $2\lambda/\tau$, (Agmon-Snir & Segev, 1993) see Fig. S4). Hence, in the uniform case where all specific parameters are equal for all cell modeled (Fig. 6), normalizing the distance in cable should equalize latency/velocity differences resulting from diameter differences.

To account for brain tissue shrinkage due to fixation, for every segment, diameter and length were scaled based on an estimation of specific neuron shrinkage (see Suppl. Table 1). To account for unequal dye spread, for a few manually picked segments, diameter value was fixed to be equal to its nearby segment (to avoid sudden diameter jump).

Equivalent cables for human and rat L2/3 PCs

"Equivalent cables" for the respective 9 modelled human and rat cells was based on Rall's cable theory (Rall, 1959). The variable diameter, $d_{eq}(X)$, of this cable as seen from the soma is,

$$(5)\ \ d_{eq}(X) = \left(\sum_j \quad d_j(X)^{3/2}\right)^{2/3}$$

where X is the cable (electrotonic) distance from the soma and $d_j(X)$ is the diameter of the jth dendrite at the distance X from that point of interest. Figure 8A shows such equivalent cables as seen from the soma. The equivalent cable for the basal tree is depicted in red and for the apical tree in blue. This enables one to graphically appreciate the large difference in the conductance load (current sink) imposed by basal tree between human and rat L2/3.

Statistical Analysis

Statistical analyses were performed in Python v.3.6, using the Python packages DABEST (Ho et al., 2019), scipy, numpy, matplotlib (Hunter, 2007), seaborn (Waskom, 2021), pandas, pinguin (Vallat, 2018), bioinfokit and scikit-learn. SHAP (Lundberg & Lee, 2017) and GLM (Kiebel & Holmes, 2007) models were done with shap python package with scikit-learn Gradient Boosting Regressor (Friedman, 2002) and with statsmodels.glm with gamma family. Interaction formula: latency ~ species + distance + radius + (species × fitted × distance) + (species × hybrid × distance) + (species × radius). No interaction: latency ~ species + distance + hybrid + radius + fitted.

Data presented as the mean ± s.d. Normality was tested with the Shapiro-Wilk test. For statistical analysis, t-test, Mann-Whitney U -test or Wilcoxon signed-rank test was used. For the statistical analyis of the drug treatmens we used two ways ANOVA with repeated measure and Tukey HSD test for posthoc comparisons. Correlations were tested using Pearson's correlation, respectively. We used the Gardner-Altman estimation plot throughout this study which is a bootstrap-coupled estimation of effect sizes, plotting the data against a mean (paired mean, as indicated) difference between the left-most condition and one or more conditions on the right (right y axis), and compared this difference against zero using 5,000 bootstrapped resamples. In these estimation graphics, each black dot indicates a mean difference, and the associated black ticks depict error bars representing 95% confidence intervals; the shaded area represents the bootstrapped sampling-error distribution

(Ho et al., 2019). Differences were accepted as significant if $p < 0.05$. The complete results of all the statistical analysis presented on the main and supplementary figures can be found as a supplementary table.

References

Agmon-Snir, H., Carr, C. E., & Rinzel, J. (1998). The role of dendrites in auditory coincidence detection. *Nature*, *393*(6682), 268–272. https://doi.org/10.1038/30505

Agmon-Snir, H., & Segev, I. (1993). Signal delay and input synchronization in passive dendritic structures. *Journal of Neurophysiology*, *70*(5), 2066–2085. https://doi.org/10.1152/jn.1993.70.5.2066

Averkin, R. G., Szemenyei, V., Bordé, S., & Tamás, G. (2016). Identified Cellular Correlates of Neocortical Ripple and High-Gamma Oscillations during Spindles of Natural Sleep. *Neuron*, *92*(4). https://doi.org/10.1016/j.neuron.2016.09.032

Ballesteros Yáñez, I., Muñoz, A., Contreras, J., Gonzalez, J., Rodriguez-Veiga, E., & DeFelipe, J. (2005). Double bouquet cell in the human cerebral cortex and a comparison with other mammals. *Journal of Comparative Neurology*, *486*(4), 344–360. https://doi.org/10.1002/cne.20533

Beaulieu-Laroche, L., Brown, N. J., Hansen, M., Toloza, E. H. S., Sharma, J., Williams, Z. M., Frosch, M. P., Cosgrove, G. R., Cash, S. S., & Harnett, M. T. (2021). Allometric rules for mammalian cortical layer 5 neuron biophysics. *Nature*, *600*(7888), 274–278. https://doi.org/10.1038/s41586-021-04072-3

Beaulieu-Laroche, L., Toloza, E. H. S., van der Goes, M. S., Lafourcade, M., Barnagian, D., Williams, Z. M., Eskandar, E. N., Frosch, M. P., Cash, S. S., & Harnett, M. T. (2018). Enhanced Dendritic Compartmentalization in Human Cortical Neurons. *Cell*, *175*(3), 643-651.e14. https://doi.org/10.1016/j.cell.2018.08.045

Benavides-Piccione, R., Regalado-Reyes, M., Fernaud-Espinosa, I., Kastanauskaite, A., Tapia-González, S., León-Espinosa, G., Rojo, C., Insausti, R., Segev, I., & Defelipe, J. (2020). Differential Structure of Hippocampal CA1 Pyramidal Neurons in the Human and Mouse. *Cerebral Cortex (New York, N.Y. : 1991)*, *30*(2), 730–752. https://doi.org/10.1093/CERCOR/BHZ122

Berg, J., Sorensen, S. A., Ting, J. T., Miller, J. A., Chartrand, T., Buchin, A., Bakken, T. E., Budzillo, A., Dee, N., Ding, S. L., Gouwens, N. W., Hodge, R. D., Kalmbach, B., Lee, C., Lee, B. R., Alfiler, L., Baker, K., Barkan, E., Beller, A., … Lein, E. S. (2021). Human neocortical expansion involves glutamatergic neuron diversification. *Nature*, *598*(7879), 151–158. https://doi.org/10.1038/S41586-021-03813-8

Bi, G. Q., & Poo, M. M. (1998). Synaptic modifications in cultured hippocampal neurons: Dependence on spike timing, synaptic strength, and postsynaptic cell type. *Journal of Neuroscience*, *18*(24), 10464–10472. https://doi.org/10.1523/jneurosci.18-24-10464.1998

Bliss, T., & Collingridge, G. (2019). Persistent memories of long-term potentiation and the N-methyl-d-aspartate receptor. *Brain and Neuroscience Advances*, *3*, 239821281984821. https://doi.org/10.1177/2398212819848213

Boldog, E., Bakken, T. E., Hodge, R. D., Novotny, M., Aevermann, B. D., Baka, J., Bordé, S., Close, J. L., Diez-Fuertes, F., Ding, S. L., Faragó, N., Kocsis, Á. K., Kovács, B., Maltzer, Z., McCorrison, J. M., Miller, J. A., Molnár, G., Oláh, G., Ozsvár, A., … Tamás, G. (2018). Transcriptomic and morphophysiological evidence for a specialized human cortical GABAergic cell type. *Nature Neuroscience*, *21*(9), 1185–1195. https://doi.org/10.1038/s41593-018-0205-2

Brent, R. (1976). A new algorithm for minimizing a function of several variables without calculating derivatives. In *Algorithms for Minimization without Derivatives* (pp. 200–248). Prentice Hall.

Buzsáki, G. (2015). Hippocampal sharp wave-ripple: A cognitive biomarker for episodic memory and planning. *Hippocampus*, *25*(10), 1073–1188. https://doi.org/10.1002/HIPO.22488

Buzsáki, G., Logothetis, N., & Singer, W. (2013). Scaling Brain Size, Keeping Timing: Evolutionary Preservation of Brain Rhythms. *Neuron*, *80*(3), 751–764. https://doi.org/10.1016/J.NEURON.2013.10.002

Buzsáki, G., & Wang, X.-J. (2012). Mechanisms of Gamma Oscillations. *Annual Review of Neuroscience*, *35*(1), 203–225. https://doi.org/10.1146/annurev-neuro-062111-150444

Cajal, S. R. y. (1899). Estudios sobre la corteza cerebral humana. *Corteza Vis Rev Trim Microgr*, *4*, 1–63.

Campagnola, L., Seeman, S. C., Chartrand, T., Kim, L., Hoggarth, A., Gamlin, C., Ito, S., Trinh, J., Davoudian, P., Radaelli, C., Kim, M. H., Hage, T., Braun, T., Alfiler, L., Andrade, J., Bohn, P., Dalley, R., Henry, A., Kebede, S., … Jarsky, T. (2022). Local connectivity and synaptic dynamics in mouse and human neocortex. *Science*, *375*(6585). https://doi.org/10.1126/science.abj5861

Caporale, N., & Dan, Y. (2008). Spike timing-dependent plasticity: A Hebbian learning rule. *Annual Review of Neuroscience*, *31*, 25–46. https://doi.org/10.1146/annurev.neuro.31.060407.125639

Chittajallu, R., Auville, K., Mahadevan, V., Lai, M., Hunt, S., Calvigioni, D., Pelkey, K. A., Zaghloul, K. A., & McBain, C. J. (2020). Activity-dependent tuning of intrinsic excitability in mouse and human neurogliaform cells. *ELife*, *9*(9), 1–30. https://doi.org/10.7554/eLife.57571

Connelly, W. M., Crunelli, V., & Errington, A. C. (2016). Passive synaptic normalization and input synchrony-dependent amplification of cortical feedback in thalamocortical neuron dendrites. *Journal of Neuroscience*, *36*(13), 3735–3754. https://doi.org/10.1523/JNEUROSCI.3836-15.2016

Dalügge, D., & Remy, S. (2018). Human Cortical Dendrites: Stretched to Perform Better? *Cell*, *175*(3), 635–637. https://doi.org/10.1016/j.cell.2018.09.052

Dan, Y., & Poo, M. M. (2004). Spike timing-dependent plasticity of neural circuits. *Neuron*, *44*(1), 23–30. https://doi.org/10.1016/j.neuron.2004.09.007

Debanne, D., Inglebert, Y., & Russier, M. (2019). Plasticity of intrinsic neuronal excitability. *Current Opinion in Neurobiology*, *54*, 73–82. https://doi.org/10.1016/J.CONB.2018.09.001

DeFelipe, J. (2011). The evolution of the brain, the human nature of cortical circuits, and intellectual creativity. *Frontiers in Neuroanatomy*, *5*(MAY). https://doi.org/10.3389/FNANA.2011.00029

Deitcher, Y., Eyal, G., Kanari, L., Verhoog, M. B., Atenekeng Kahou, G. A., Mansvelder, H. D., De Kock, C. P. J., & Segev, I. (2017). Comprehensive Morpho-Electrotonic Analysis Shows 2 Distinct Classes of L2 and L3 Pyramidal Neurons in Human Temporal Cortex. *Cerebral Cortex*, *27*(11), 5398–5414. https://doi.org/10.1093/CERCOR/BHX226

Eyal, G., Mansvelder, H. D., de Kock, C. P. J., & Segev, I. (2014). Dendrites impact the encoding capabilities of the axon. *Journal of Neuroscience*, *34*(24), 8063–8071. https://doi.org/10.1523/JNEUROSCI.5431-13.2014

Eyal, G., Verhoog, M. B., Testa-Silva, G., Deitcher, Y., Lodder, J. C., Benavides-Piccione, R., Morales, J., DeFelipe, J., de Kock, C. P. J., Mansvelder, H. D., & Segev, I. (2016). Unique membrane properties and enhanced signal processing in human neocortical neurons. *ELife*, *5*(OCTOBER2016), 1–18. https://doi.org/10.7554/eLife.16553

Fedchyshyn, M. J., & Wang, L. Y. (2007). Activity-dependent changes in temporal components of neurotransmission at the juvenile mouse calyx of Held synapse. *The Journal of Physiology*, *581*(Pt 2), 581–602. https://doi.org/10.1113/JPHYSIOL.2007.129833

Feldman, D. E. (2012). The Spike-Timing Dependence of Plasticity. *Neuron*, *75*(4), 556–571. https://doi.org/10.1016/j.neuron.2012.08.001

Fişek, M., & Häusser, M. (2020). Are Human Dendrites Different? *Trends in Cognitive Sciences*, *24*(6), 411–412. https://doi.org/10.1016/j.tics.2020.03.002

Frick, A., Feldmeyer, D., Helmstaedter, M., & Sakmann, B. (2008). Monosynaptic connections between pairs of L5A pyramidal neurons in columns of juvenile rat somatosensory cortex. *Cerebral Cortex (New York, N.Y. : 1991)*, *18*(2), 397–406. https://doi.org/10.1093/cercor/bhm074

Friedman, J. H. (2002). Stochastic gradient boosting. In *Computational Statistics & Data Analysis* (Vol. 38). www.elsevier.com/locate/csda

Galakhova, A. A., Hunt, S., Wilbers, R., Heyer, D. B., de Kock, C. P. J., Mansvelder, H. D., & Goriounova, N. A. (2022). Evolution of cortical neurons supporting human cognition. *Trends in Cognitive Sciences*. https://doi.org/10.1016/J.TICS.2022.08.012

Gentet, L. J., Stuart, G. J., & Clements, J. D. (2000). Direct measurement of specific membrane capacitance in neurons. *Biophysical Journal*, *79*(1), 314–320. https://doi.org/10.1016/S0006-3495(00)76293-X

Gidon, A., Zolnik, T. A., Fidzinski, P., Bolduan, F., Papoutsi, A., Poirazi, P., Holtkamp, M., Vida, I., & Larkum, M. E. (2020). Dendritic action potentials and computation in human layer 2/3 cortical neurons. *Science (New York, N.Y.)*, *367*(6473), 83–87. https://doi.org/10.1126/SCIENCE.AAX6239

Gooch, H. M., Bluett, T., Perumal, M. B., Vo, H. D., Fletcher, L. N., Papacostas, J., Jeffree, R. L., Wood, M., Colditz, M. J., McMillen, J., Tsahtsarlis, T., Amato, D., Campbell, R., Gillinder, L., & Williams, S. R. (2022). High-fidelity dendritic sodium spike generation in human layer 2/3 neocortical pyramidal neurons. *Cell Reports*, *41*(3), 111500. https://doi.org/10.1016/j.celrep.2022.111500

Goriounova, N. A., Heyer, D. B., Wilbers, R., Verhoog, M. B., Giugliano, M., Verbist, C., Obermayer, J., Kerkhofs, A., Smeding, H., Verberne, M., Idema, S., Baayen, J. C., Pieneman, A. W., de Kock, C. P. J., Klein, M., & Mansvelder, H. D. (2018). Large and fast human pyramidal neurons associate with intelligence. *ELife*, *7*. https://doi.org/10.7554/ELIFE.41714

Hay, E., Gidon, A., London, M., & Segev, I. (2016). A theoretical view of the neuron as an input–output computing device. In G. Stuart, N. Spruston, & M. Häusser (Eds.), *Dendrites* (pp. 439–464). Oxford University Press. https://doi.org/10.1093/acprof:oso/9780198745273.003.0015

Hebb, D. O. (1949). The Organization of Behavior. In *The Organization of Behavior*. John Wiley and Sons.

Herculano-Houzel, S. (2011). Not all brains are made the same: new views on brain scaling in evolution. *Brain, Behavior and Evolution*, *78*(1), 22–36. https://doi.org/10.1159/000327318

Hines, M. L., Davison, A. P., & Muller, E. (2009). NEURON and Python. *Frontiers in Neuroinformatics*, *3*(JAN). https://doi.org/10.3389/NEURO.11.001.2009

Ho, J., Tumkaya, T., Aryal, S., Choi, H., & Claridge-Chang, A. (2019). Moving beyond P values: data analysis with estimation graphics. *Nature Methods*, *16*(7), 565–566. https://doi.org/10.1038/s41592-019-0470-3

Hunt, S., Leibner, Y., Mertens, E. J., Barros-Zulaica, N., Kanari, L., Heistek, T. S., Karnani, M. M., Aardse, R., Wilbers, R., Heyer, D. B., Goriounova, N. A., Verhoog, M. B., Testa-Silva, G., Obermayer, J., Versluis, T., Benavides-Piccione, R., de Witt-Hamer, P., Idema, S., Noske, D. P., … de Kock, C. P. J. (2022). Strong and

reliable synaptic communication between pyramidal neurons in adult human cerebral cortex. *Cerebral Cortex*, 1–22. https://doi.org/10.1093/cercor/bhac246

Hunter, J. D. (2007). Matplotlib: A 2D graphics environment. *Computing in Science and Engineering*, *9*(3), 90–95. https://doi.org/10.1109/MCSE.2007.55

Jack, J. J. B., Noble, D., & Tsien, R. W. (1975). *Electric current flow in excitable cells*. Clarendon Press .

Kalmbach, B. E., Buchin, A., Long, B., Close, J., Nandi, A., Miller, J. A., Bakken, T. E., Hodge, R. D., Chong, P., de Frates, R., Dai, K., Maltzer, Z., Nicovich, P. R., Keene, C. D., Silbergeld, D. L., Gwinn, R. P., Cobbs, C., Ko, A. L., Ojemann, J. G., … Ting, J. T. (2018). h-Channels Contribute to Divergent Intrinsic Membrane Properties of Supragranular Pyramidal Neurons in Human versus Mouse Cerebral Cortex. *Neuron*, *100*(5), 1194-1208.e5. https://doi.org/10.1016/j.neuron.2018.10.012

Kiebel, S. J., & Holmes, A. P. (2007). The General Linear Model. In K. Friston, J. Ashburner, S. Kiebel, T. Nichols, & P. William (Eds.), *Statistical Parametric Mapping* (pp. 101–125). Academic Press.

Klinzing, J. G., Niethard, N., & Born, J. (2019). Mechanisms of systems memory consolidation during sleep. *Nature Neuroscience 2019 22:10*, *22*(10), 1598–1610. https://doi.org/10.1038/s41593-019-0467-3

Komlósi, G., Molnár, G., Rózsa, M., Oláh, S., Barzó, P., & Tamás, G. (2012). Fluoxetine (Prozac) and serotonin act on excitatory synaptic transmission to suppress single layer 2/3 pyramidal neuron-triggered cell assemblies in the human prefrontal cortex. *Journal of Neuroscience*, *32*(46), 16369–16378. https://doi.org/10.1523/JNEUROSCI.2618-12.2012

Kullmann, D. M., Moreau, A. W., Bakiri, Y., & Nicholson, E. (2012). Plasticity of Inhibition. *Neuron*, *75*(6), 951–962. https://doi.org/10.1016/j.neuron.2012.07.030

Laughlin, S. B., & Sejnowski, T. J. (2003). Communication in neuronal networks. *Science*, *301*(5641), 1870–1874. https://doi.org/10.1126/science.1089662

London, M., & Häusser, M. (2005). Dendritic Computation. *Annual Review of Neuroscience*, *28*(1), 503–532. https://doi.org/10.1146/annurev.neuro.28.061604.135703

Loomba, S., Straehle, J., Gangadharan, V., Heike, N., Khalifa, A., Motta, A., Ju, N., Sievers, M., Gempt, J., Meyer, H. S., & Helmstaedter, M. (2022). Connectomic comparison of mouse and human cortex. *Science*, *377*(6602). https://doi.org/10.1126/SCIENCE.ABO0924/SUPPL_FILE/SCIENCE.ABO0924_MDAR_REPRODUCIBILITY_CHECKLIST.PDF

Lundberg, S. M., & Lee, S.-I. (2017). A unified approach to interpreting model predictions. *Proceedings of the 31st International Conference on Neural Information Processing Systems*, 4768–4777.

Malenka, R. C., & Bear, M. F. (2004). LTP and LTD: An embarrassment of riches. *Neuron*, *44*(1), 5–21. https://doi.org/10.1016/j.neuron.2004.09.012

Manor, Y., Koch, C., & Segev, I. (1991). Effect of geometrical irregularities on propagation delay in axonal trees. *Biophysical Journal*, *60*(6), 1424–1437. https://doi.org/10.1016/S0006-3495(91)82179-8

Mansvelder, H. D., Verhoog, M. B., & Goriounova, N. A. (2019). Synaptic plasticity in human cortical circuits: cellular mechanisms of learning and memory in the human brain? *Current Opinion in Neurobiology*, *54*, 186–193. https://doi.org/10.1016/j.conb.2018.06.013

Markram, H., Gerstner, W., & Sjöström, P. J. (2012). Spike-timing-dependent plasticity: a comprehensive overview. *Frontiers in Synaptic Neuroscience*, *4*(JULY). https://doi.org/10.3389/FNSYN.2012.00002

Markram, H., Lübke, J., Frotscher, M., & Sakmann, B. (1997). Regulation of synaptic efficacy by coincidence of postsynaptic APs and EPSPs. *Science*, *275*(5297), 213–215. https://doi.org/10.1126/science.275.5297.213

Markram, H., & Sakmann, B. (1994). Calcium transients in dendrites of neocortical neurons evoked by single subthreshold excitatory postsynaptic potentials via low-voltage-activated calcium channels. *Proceedings of the National Academy of Sciences of the United States of America*, *91*(11), 5207–5211. https://doi.org/10.1073/pnas.91.11.5207

Mohan, H., Verhoog, M. B., Doreswamy, K. K., Eyal, G., Aardse, R., Lodder, B. N., Goriounova, N. A., Asamoah, B., B. Brakspear, A. B. C., Groot, C., Van Der Sluis, S., Testa-Silva, G., Obermayer, J., Boudewijns, Z. S. R. M., Narayanan, R. T., Baayen, J. C., Segev, I., Mansvelder, H. D., & De Kock, C. P. J. (2015). Dendritic and axonal architecture of individual pyramidal neurons across layers of adult human neocortex. *Cerebral Cortex*, *25*(12), 4839–4853. https://doi.org/10.1093/cercor/bhv188

Molnár, G., Oláh, S., Komlósi, G., Füle, M., Szabadics, J., Varga, C., Barzó, P., & Tamás, G. (2008). Complex events initiated by individual spikes in the human cerebral cortex. *PLoS Biology*, *6*(9), 1842–1849. https://doi.org/10.1371/journal.pbio.0060222

Molnár, G., Rózsa, M., Baka, J., Holderith, N., Barzó, P., Nusser, Z., & Tamás, G. (2016). Human pyramidal to interneuron synapses are mediated by multi-vesicular release and multiple docked vesicles. *ELife*, *5*(AUGUST), 1–12. https://doi.org/10.7554/eLife.18167

Nádasdy, Z., Hirase, H., Czurkó, A., Csicsvari, J., & Buzsáki, G. (1999). Replay and time compression of recurring spike sequences in the hippocampus. *Journal of Neuroscience*, *19*(21), 9497–9507. https://doi.org/10.1523/jneurosci.19-21-09497.1999

Oberheim, N. A., Takano, T., Han, X., He, W., Lin, J. H. C., Wang, F., Xu, Q., Wyatt, J. D., Pilcher, W., Ojemann, J. G., Ransom, B. R., Goldman, S. A., & Nedergaard, M. (2009). Uniquely Hominid Features of Adult Human Astrocytes. *Journal of Neuroscience*, *29*(10), 3276–3287. https://doi.org/10.1523/JNEUROSCI.4707-08.2009

Palmer, L. M., & Stuart, G. J. (2006). Site of action potential initiation in layer 5 pyramidal neurons. *Journal of Neuroscience*, *26*(6), 1854–1863. https://doi.org/10.1523/JNEUROSCI.4812-05.2006

Rall, W. (1959). Branching dendritic trees and motoneuron membrane resistivity. *Experimental Neurology*, *1*(5), 491–527. https://doi.org/10.1016/0014-4886(59)90046-9

Rall, W. (1964). Theoretical significance of dendritic trees and motoneuron input-output relations. In R. F. Reiss (Ed.), *Neural Theory and Modeling* (Issue September, pp. 122–146). Palo Alto: Stanford University Press.

Rall, W., & Rinzel, J. (1973). Branch Input Resistance and Steady Attenuation for Input to One Branch of a Dendritic Neuron Model. *Biophysical Journal*, *13*(7), 648–688. https://doi.org/10.1016/S0006-3495(73)86014-X

Rinzel, J., & Rall, W. (1974). Transient Response in a Dendritic Neuron Model for Current Injected at One Branch. *Biophysical Journal*, *14*(10), 759–790. https://doi.org/10.1016/S0006-3495(74)85948-5

Roome, C. J., & Kuhn, B. (2018). Simultaneous dendritic voltage and calcium imaging and somatic recording from Purkinje neurons in awake mice. *Nature Communications*, *9*(1), 1–14. https://doi.org/10.1038/s41467-018-05900-3

Segev, I., Fleshman, J. W., & Burke, R. E. (1989). Compartmental models of complex neurons. In *Methods in Neuronal Modeling: From Synapses to Networks* (pp. 63–96). MIT Press.

Skaggs, W. E., & McNaughton, B. L. (1996). Replay of neuronal firing sequences in rat hippocampus during sleep following spatial experience. *Science (New York, N.Y.)*, *271*(5257), 1870–1873. https://doi.org/10.1126/SCIENCE.271.5257.1870

Spruston, N., Stuart, G., & Häusser, M. (2016). Principles of dendritic integration. *Dendrites*, 351–398. https://doi.org/10.1093/acprof:oso/9780198745273.003.0012

Stuart, G. J., & Sakmann, B. (1994). Active propagation of somatic action potentials into neocortical pyramidal cell dendrites. *Nature*, *367*, 69–72. https://doi.org/10.1038/367069a0

Szegedi, V., Paizs, M., Csakvari, E., Molnar, G., Barzo, P., Tamas, G., & Lamsa, K. (2016). Plasticity in Single Axon Glutamatergic Connection to GABAergic Interneurons Regulates Complex Events in the Human Neocortex. *PLoS Biology*, *14*(11), 1–21. https://doi.org/10.1371/journal.pbio.2000237

Vallat, R. (2018). Pingouin: statistics in Python. *Journal of Open Source Software*, *3*(31), 1026. https://doi.org/10.21105/joss.01026

Van Quyen, M. Le, Muller, L. E., Telenczuk, B., Halgren, E., Cash, S., Hatsopoulos, N. G., Dehghani, N., & Destexhe, A. (2016). High-frequency oscillations in human and monkey neocortex during the wake-sleep cycle. *Proceedings of the National Academy of Sciences of the United States of America*, *113*(33), 9363–9368. https://doi.org/10.1073/PNAS.1523583113/SUPPL_FILE/PNAS.1523583113.SM03.MP4

Vaz, A. P., Wittig, J. H., Inati, S. K., & Zaghloul, K. A. (2020). Replay of cortical spiking sequences during human memory retrieval. *Science*, *367*(6482), 1131–1134. https://doi.org/10.1126/SCIENCE.AAZ3691

Verhoog, M. B., Goriounova, N. A., Obermayer, J., Stroeder, J., Johannes Hjorth, J. J., Testa-Silva, G., Baayen, J. C., de Kock, C. P. J., Meredith, R. M., & Mansvelder, H. D. (2013). Mechanisms underlying the rules for associative plasticity at adult human neocortical synapses. *Journal of Neuroscience*, *33*(43), 17197–17208. https://doi.org/10.1523/JNEUROSCI.3158-13.2013

Vetter, P., Roth, A., & Häusser, M. (2001). Propagation of action potentials in dendrites depends on dendritic morphology. *Journal of Neurophysiology*, *85*(2), 926–937. https://doi.org/10.1152/jn.2001.85.2.926

Wang, S. S. H., Denk, W., & Häusser, M. (2000). Coincidence detection in single dendritic spines mediated by calcium release. *Nature Neuroscience*, *3*(12), 1266–1273. https://doi.org/10.1038/81792

Ward, L. M. (2003). Synchronous neural oscillations and cognitive processes. *Trends in Cognitive Sciences*, *7*(12), 553–559. https://doi.org/10.1016/J.TICS.2003.10.012

Waskom, M. (2021). seaborn: statistical data visualization. *Journal of Open Source Software*, *6*(60), 3021. https://doi.org/10.21105/joss.03021

Waxman, S. G., & Bennett, M. V. L. (1972). Relative Conduction Velocities of Small Myelinated and Non-myelinated Fibres in the Central Nervous System. *Nature New Biology*, *238*(85), 217–219. https://doi.org/10.1038/newbio238217a0

West, G. B., Brown, J. H., & Enquist, B. J. (1997). A general model for the origin of allometric scaling laws in biology. *Science (New York, N.Y.)*, *276*(5309), 122–126. https://doi.org/10.1126/SCIENCE.276.5309.122

Wilson, M. A., & McNaughton, B. L. (1994). Reactivation of hippocampal ensemble memories during sleep. *Science*, *265*(5172), 676–679. https://doi.org/10.1126/science.8036517

Acknowledgments

The authors thank Éva Tóth, Katalin Kocsis, Leona Mezei and Bettina Lehóczki for assistance in anatomical experiments, Judith Baka for providing the electron micrographs for membrane thickness measurements, Gergely Komlósi, Martin Tóth, Miklós Füle, Szabina Furdan, Szabolcs Oláh, Zoltán Péterfi for recording some neuron and Attila Ozsvár, Márton Rózsa, Martin Tóth, Ildikó Szöts, Norbert Mihut, Róbert Averkin, Sándor Bordé, Viktor Szegedi for useful feedback and suggestions. The technical help and methodical suggestions of János Szabadics, János Brunner and Viktor Oláh at the beginning of the project are appreciated. This work is dedicated to the memory of Mrs. Lily Safra, a great supporter of brain research.

Funding:
This work was supported by Eötvös Loránd Research Network grants ELKH-SZTE Agykérgi Neuronhálózatok Kutatócsoport and KÖ-36/2021 (G.T.)

Ministry of Human Capacities Hungary (20391-3/2018/FEKUSTRAT and NKP 16-3-VIII-3) (G.T.);

National Research, Development and Innovation Office grants GINOP 2.3.2-15-2016-00018, Élvonal KKP 133807, ÚNKP-20-5 - SZTE-681, 2019-2.1.7-ERA-NET-2022-00038, TKP2021-EGA-09, TKP-2021-EGA-28 (G.T.) and OTKA K128863 (G.T., G.M.)

ÚNKP-21-5-SZTE-580 New National Excellence Program of the Ministry for Innovation and Technology from the source of the National Research, Development and Innovation Fund (G.M.)

ÚNKP 16-3-VIII-3 new national excellence program of the Ministry of Human Capacities (G.O.)

János Bolyai Research Scholarship of the Hungarian Academy of Sciences (G.M.)

Hungarian Scientific Research Foundation under grant ANN-135291 (A.Sz.)

National Institutes of Health awards U01MH114812 (G.T., I.S.) and UM1MH130981 (G.T.)

The Patrick and Lina Drahi Foundation, grant from the ETH domain for the Blue Brain Project, the Gatsby Charitable Foundation (I.S.).

Author contributions:

Conceptualization: GT, IS, GM, GO
Methodology: GO, GM, RL, AS, PB, EC, SS, YL, IS, GT
Investigation: GO, GM, RL, AS, PB, EC, SS, YL
Visualization: GO, GM, SS
Supervision: GM, IS, GT
Writing—original draft: GO, SS, GM, IS, GT
Writing—review & editing: GO, SS, GM, IS, GT

Competing interests: Authors declare that they have no competing interests.

Data and materials availability: All data, code, and materials used in the analyses is available upon request following publication.

Figure legends and Tables

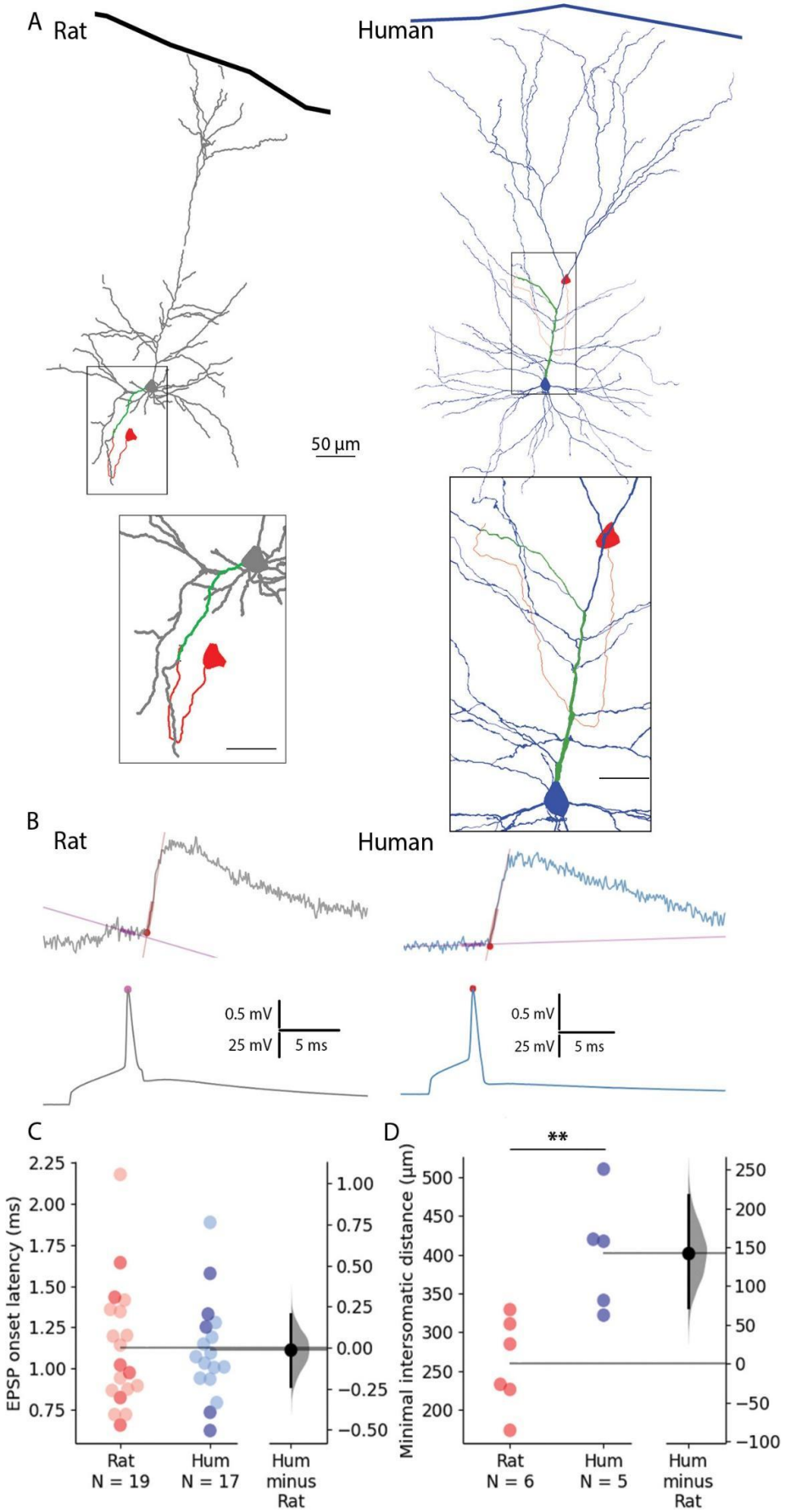

Fig.1. Paired recordings from synaptically connected layer 2/3 rat and human pyramidal cells. A Representative reconstructions of electrophysiologically recorded and biocytin filled rat (left, gray soma and dendrites) and human (right, blue soma and dendrites) synaptically connected pyramidal cell pairs. The presynaptic soma and the axon are in red; the postsynaptic dendritic path from the synapse to the soma is highlighted in green. Minimal intersomatic distance was calculated as the sum of the shortest presynaptic axonal (red) and postsynaptic dendritic (green) paths. Boxed region is magnified on the bottom. Scale bars for insets are 20 µm. **B** Synaptic latency was determined as the time difference between the peak of the presynaptic AP (pink dot) and the onset of the postsynaptic excitatory postsynaptic potential (red dot). Straight lines indicate baseline and rise phase fitting. **C** Summary of synaptic latencies in rat (red) and human (blue) cell pair recordings. Each dot represents the average latency in a cell measured from the AP peak to EPSP onset as illustrated in panel B. The darker colors represent the paired recordings with full reconstruction. For these data points there was no significant difference between the two species (Mann-Whitney test: $P = 0.931$). The extended dataset with cell pairs without reconstruction shows no significant difference between the two species (Mann-Whitney test: $P = 0.949$). **D** Minimal intersomatic distance of the recorded cell pairs. Intersomatic distance was calculated through every putative synapse and the shortest was taken into account. The minimal intersomatic distance was significantly longer in the human dataset compared to rats (Mann-Whitney test: $P = 0.009$). $^{**}P < 0.01$.

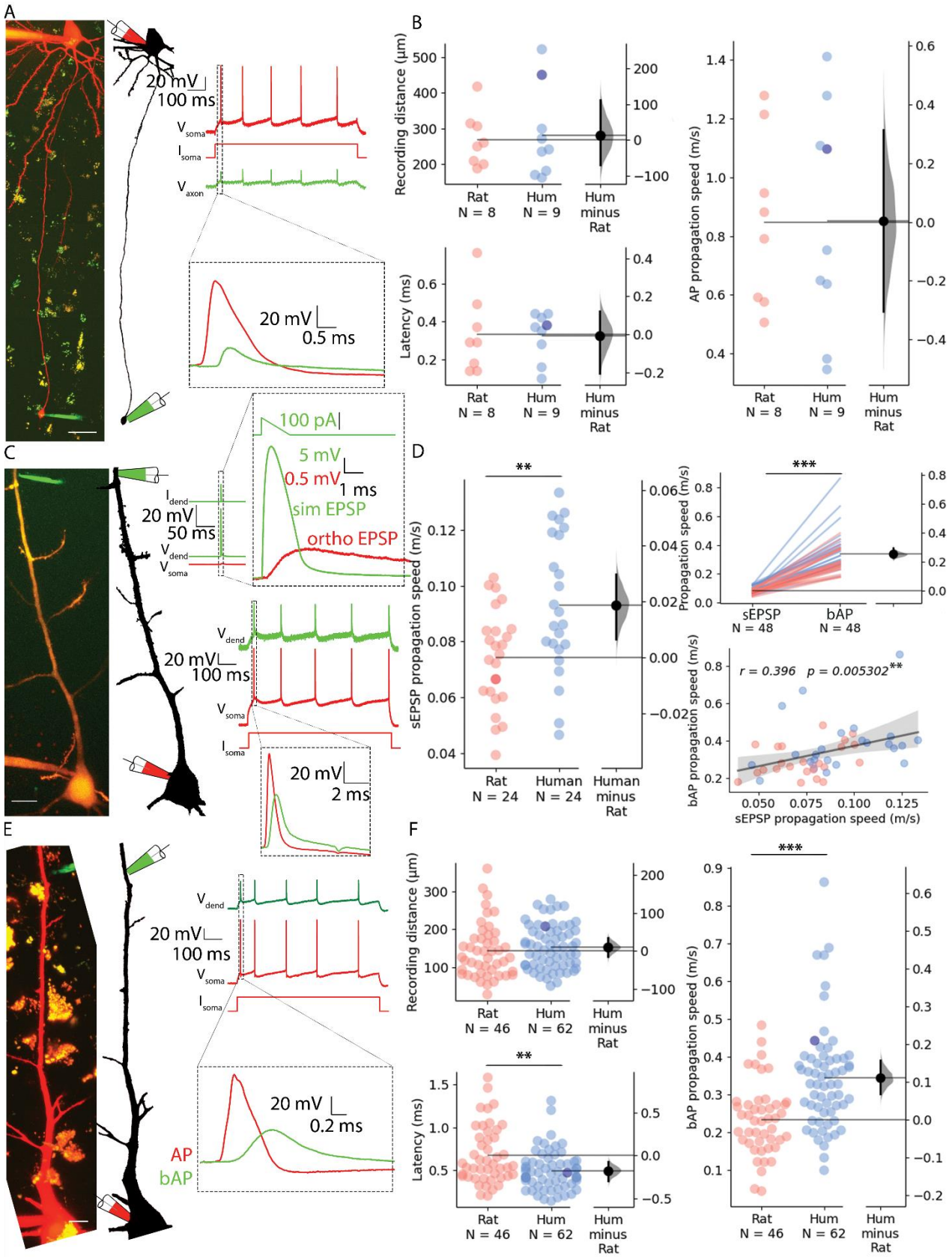

Fig. 2. Propagation velocity of dendritic and axonal signals in rat and human cortical pyramidal cells. **A** Left, Human pyramidal cell simultaneously recorded with a somatic (red pipette) and axonal (green pipette) electrode. Right, Somatic depolarizing current (I_{soma}) evoked action potentials (V_{soma}) and their propagation to the axonal recording site (V_{axon}). **B** Path distances and AP latencies measured between the soma and axon bleb. AP propagation speed measured along the axon showed no significant difference (two sample *t* test: P = 0.986). All

recordings were made at resting membrane potential. **C** Left, Two-photon image of a rat pyramidal cell recorded simultaneously with a somatic (red pipette) and dendritic (green pipette) electrode. Top, Dendritic stimulation (I_{dend}) with simulated EPSP waveform (V_{dend}) and somatic response (V_{soma}). Bottom, Somatic stimulation (I_{soma}) triggers an AP (V_{soma}) detected in the dendrite as bAP (V_{dend}). **D** Left, simulated EPSP propagation speed in rat and human cells (rat: 0.074 ± 0.018 m/s vs. human: 0.093 ± 0.025 m/s, two sample *t* test: P = 0.004). Top right, simulated EPSP dendritic propagation speed was lower than bAP propagation speed (sEPSP: 0.084 ± 0.023 m/s vs. bAP: 0.337 ± 0.128 m/s, Wilcoxon signed ranks test: $P = 1.631\times10^{-9}$). Bottom right: there was a significant correlation in the forward propagating sEPSP speed and the speed of bAPs. Darker dot is the data for the cell shown on panel C. **E** Left, Two-photon image and reconstruction of a human pyramidal cell recorded simultaneously with a somatic (red pipette) and dendritic (green pipette) electrode. Right, Somatic current (I_{soma}) evoked APs (V_{soma}) and their backpropagation into the dendritic recording site (V_{dend}). **F** Top left, recording distance. Lower left, bAP latency was shorter in human cells (Mann-Whitney test: P=0.005). Right, bAP propagation speed was significantly higher in human dendrites (Mann-Whitney test: $P = 6.369\times10^{-6}$). Darker dot indicate the data for the cell shown on panel E. Scale bars A and C: 10 µm, E: 20 µm.*P<0.05, **P<0.01, ***P<0.001

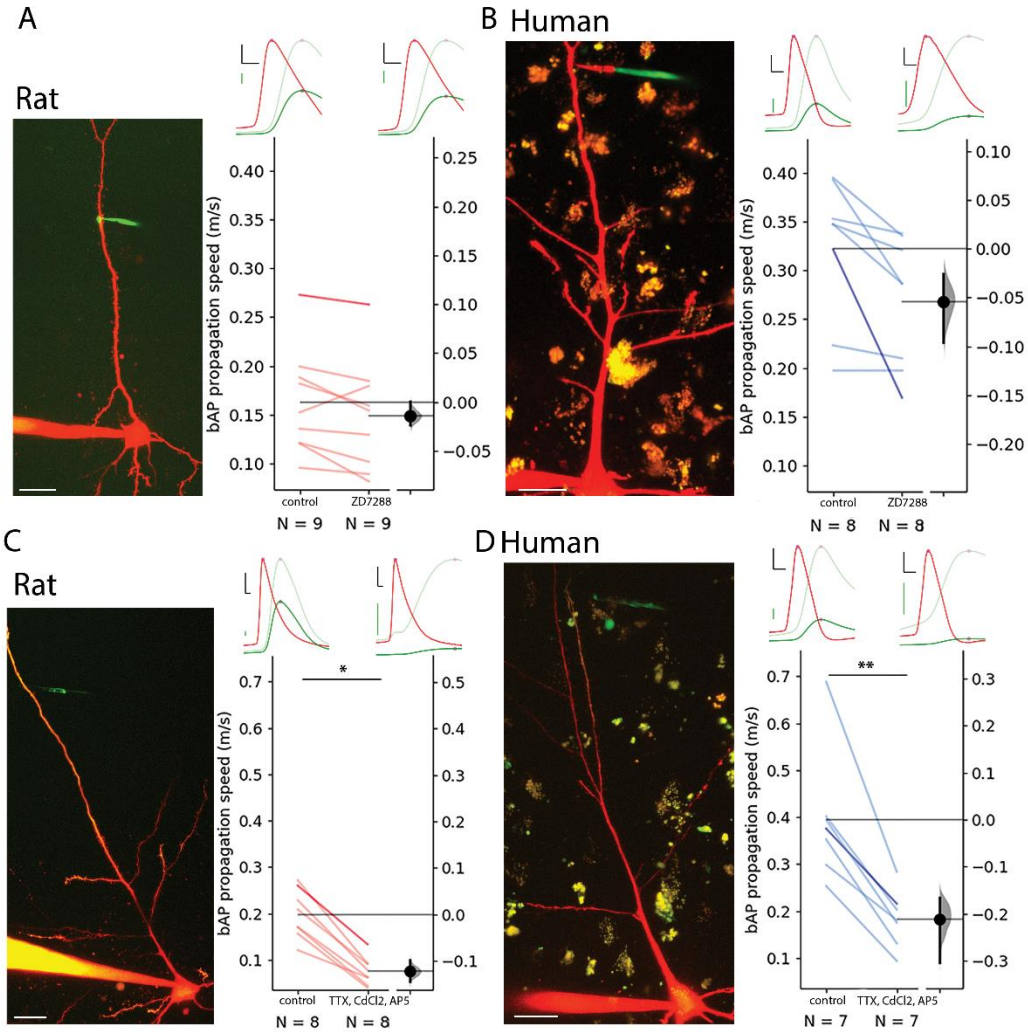

Fig. 3. Contribution of HCN, Ca^{2+}, Na^{+} and NMDA channels to bAP propagation speed in rat and human dendrites. A Representative recording from layer 2/3 pyramidal cell of a rat. Two-photon maximum intensity projection image of Alexa 594 and biocytin filled neuron on the left, representative somatic AP (red) and dendritic bAP (green) on the upper right in the control condition (left) and after 20 µM ZD7288 application (right). The light green represents the dendritic signal scaled to the amplitude of the somatic signal for better visibility. Effect of ZD7288 on bAP propagation speed. Darker color represents the example cell. **B** Same as in panel A but for human cells. **C-D** Same as A and B but the ACSF contained 1 µM TTX, 200 µM $CdCl_2$, and 20 µM AP5 in the drug application condition. Black scale bars 20 mV and 0.3 ms. Green scale bars 5 mV on A and B, 2.5 mV on C and D. Scale bars on microphotographs 20 µm. All recordings were done on resting membrane potential. *P < 0.05, **P < 0.01.

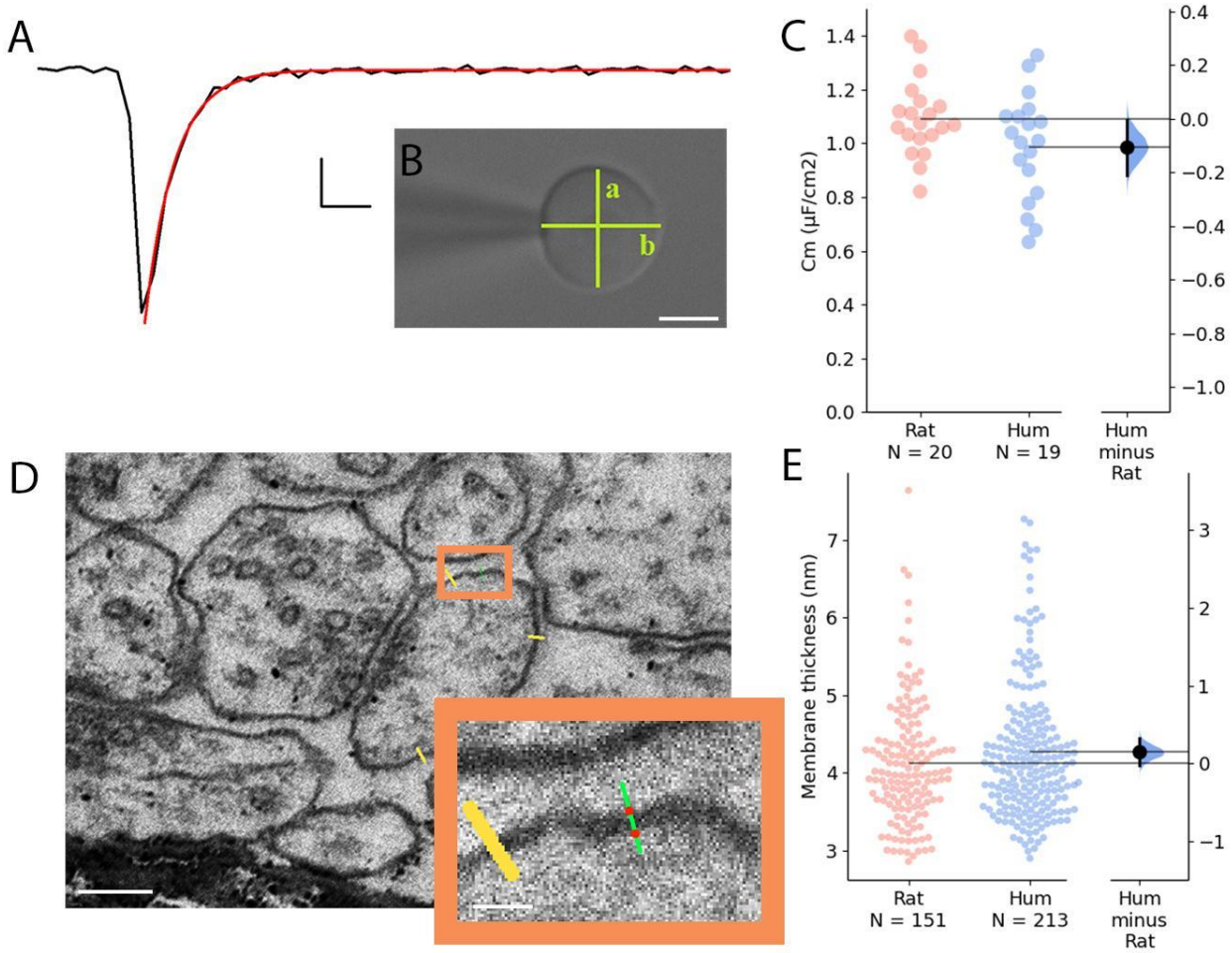

Fig. 4. Comparative analysis of membrane capacitance and thickness in rat and human cortex
A Representative capacitive transient of a nucleated patch pulled from layer 2/3 neocortical pyramidal cell (black). A single exponential function was fitted on the measured signal (red) for the calculation of the time constant of the membrane. Scale bar: 100 pA, 20 µs. **B** Differential interference contrast microscope image of a neuronal nucleus. The shortest (a) and longest (b) diameter values were used to calculate the membrane surface. Scale bar 5 µm. **C** Specific membrane capacitance of rat (red) and human (blue) neocortical pyramidal cells. **D** Electron micrographs of dendritic membranes used for membrane thickness measurements. Yellow lines indicate measuring profiles. Scale bar 40 nm. Boxed region magnified on the right. The two red dots on the green line show the edges of the membrane (see methods). Inset scale bar 10 nm. **E** Membrane thickness of rat (red, n = 151 from n = 3 rat) and human (blue, n = 213 from n = 3 patient) neocortical cell dendrites (Mann-Whitney test: P = 0.212).

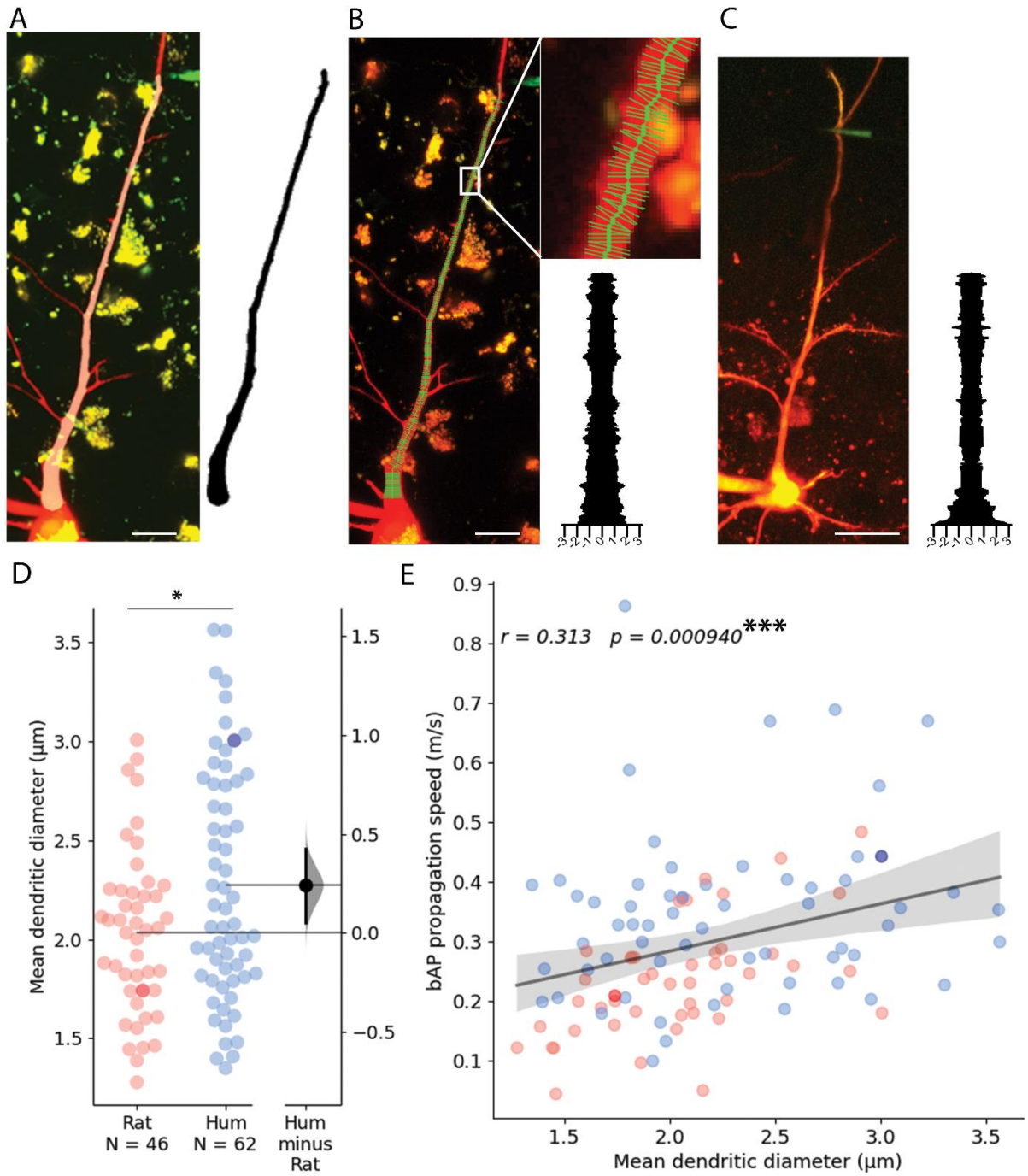

Fig. 5. Dendritic thickness reconstructions and comparison of layer 2/3 pyramidal cells in the human and rat cortex. A Left, Maximum intensity projection of Alexa594 and biocytin filled human pyramidal cell imaged in two-photon microscope. Right, model of 3D reconstructed apical dendrite. Middle, overlay of the two-photon image and the model. **B** Apical dendrite thickness measurements on the sample shown in A. Left, The center of the dendrite is tracked by a thick green line while the perpendicular thin lines show measured profiles. Right, Stacked thickness measurements with micrometer scale. **C** Same as in B with a rat sample. Scale bars 20 µm. **D** Comparison of rat and human apical dendrite averaged thickness. The mean dendritic diameter of human dendrites was significantly thicker than rat ones (two sample *t* test: P = 0.019). Darker dots indicate data measured on image stacks shown in panel B and C. **E** bAP propagation speed correlates significantly with dendrite thickness. Pearson correlation coefficient (r) values for fitted lines are shown on the upper left corner of the plot. The shaded area around the regression line shows the 0-100 % confidence interval for the bootstrapped data. *** P < 0.001.

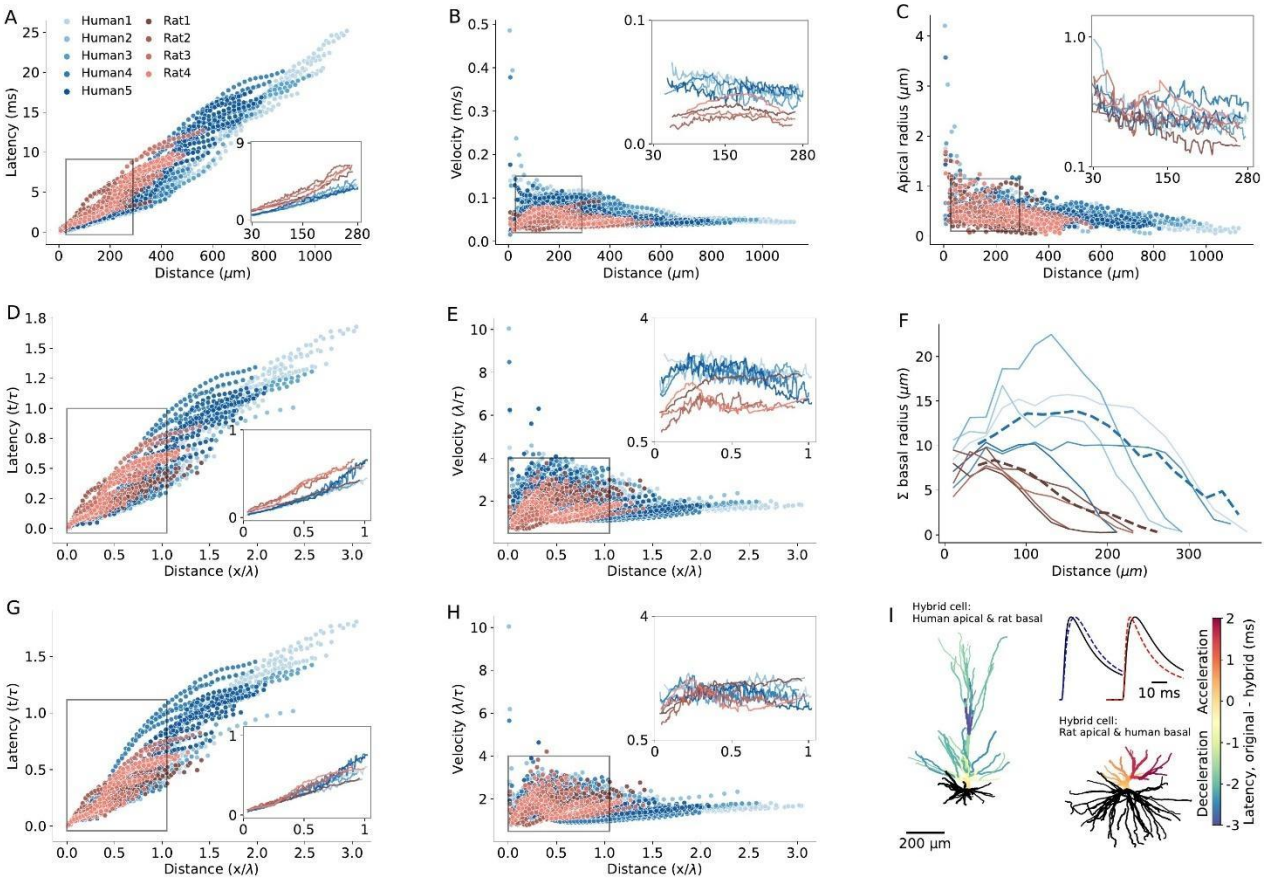

Fig. 6. Modeling explains the enhanced EPSPs velocity in the apical dendrites of human L2/3 PCs. A Latency and **B**, velocity of EPSP in models of 5 human (blue) and 4 rat (red) reconstructed L2/3 PCs. Insets show the respective averages for the zoom-in region (box), which brackets the experimental range of dendritic recordings. Note the smaller latency and larger velocity in human PCs. **C**. Dendritic radius as a function of distance from the soma. Note the larger radius of human dendrites in the outlined region. **D,E** As A and B, but now distance is normalized in cable units (thus incorporating the diameters differences between cells) and time is normalized in units of membrane time constant. **F** Sum of radii of basal dendrites as a function of distance from the soma (blue – human, red – rat), in 20μm bins. Dashed lines are the respective averages. **G-H** As D and E but for 'hybrid cells', computed for the 5 modeled human neurons, all having the basal tree of 'Rat4' (blue) and for the 4 modeled rat cells, all with the basal tree of 'Rat4' (red). Note that the differences in latency and velocity between human and rat diminished (insets). **I** Two examples of a color-coded "latency-gram", visualizing the effect of replacing the basal tree of human L2/3 PC with the basal tree of rat L2/3 PC and *vice versa*. Top left: "Human1" apical tree with basal tree (in black) of "Rat4" PC. Lower left: "Rat4" apical tree with basal tree of "Human1". Color-coded difference in latency was calculated by subtracting the respective values of the original cells from those calculated for the "hybrid cells". The blueish apical tree of the human apical tree indicates deceleration whereas the reddish apical tree of the rat PC indicates acceleration of the EPSPs. Inset shows examples of a somatic EPSP's in these two cases. Shown are the original EPSPs (black lines) and the EPSPs computed for the respective hybrid cases (dashed line in blue – deceleration; dashed red line – acceleration) both for synaptic inputs at 288 μm from soma. Specific cable properties in all cells were: $C_m = 1$ μF/cm^2, $R_m = 15{,}000$ Ωcm^2, $R_a = 150$ Ωcm.

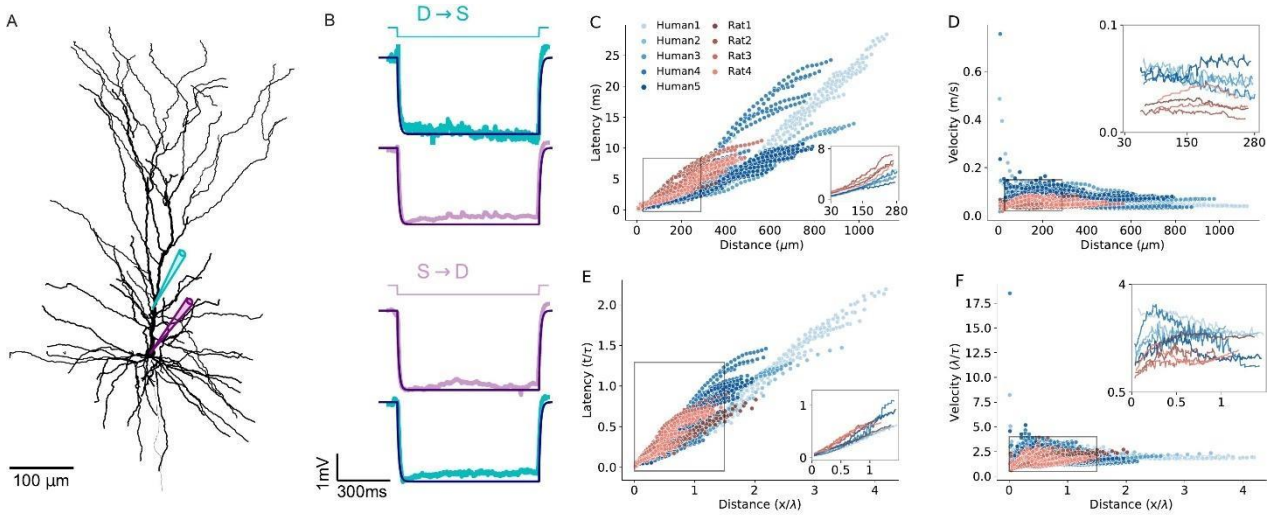

Fig. 7. Modeling EPSPs latency and velocity in dendrites of human and rat L2/3 pyramidal cells based on experimentally-fitted cable parameters. A Exemplar modeled ("Human5") L2/3 PC, also showing the locations of the two recording/stimulating electrodes. **B** Top (D→S): step hyperpolarizing current (-100 pA) injected to the dendrite of the modeled cell (cyan). Lower trace: Model fit (dark purple line) to the voltage response at the soma (noisy light purple line). The resultant fit to the local dendritic voltage response is also shown (in cyan). Bottom (S→D): as is the case at top, but with current step injected to the soma (purple step current). This fitting procedure resulted with the following passive parameters: C_m = 0.63 $\mu F/cm^2$, R_m = 15,570 Ωcm^2, R_a = 109 Ωcm. **C** Latency and **D** Velocity of EPSPs for the 9 model cells as in Figure 6A,B, but now with specific cable parameters fitted to the individual modeled neurons (see Table 1). **E-F** As in C and D, with distance normalized in cable units and time normalized by the membrane time constant (see Table 2). Note the smaller latency and larger velocity for the human PCs, which is now more significant as compared to the case where the cable parameters were uniform for all modeled cells (compare to Figure 6D and E).

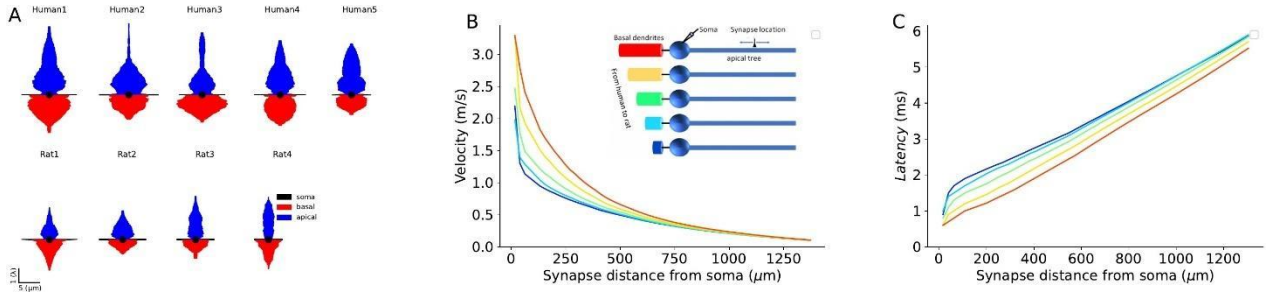

Fig. 8. Impact of conductance load of the basal tree on EPSPs velocity and latency. A Equivalent cable for the apical tree (in blue) and the basal tree (in red) for the 9 L2/3 cells modeled in this study. Note the relatively large conductance load (sink) imposed by the large basal tree in human cells. **B** EPSP velocity and **C** latency as a function of distance of the (apical) synapse from the soma. The synapse was located along the "apical" cable (blue cylinder, inset). The respective 5 cases are shown in the inset. Velocity and latency were computed as in Figs. 6 and 7. Note the enhanced velocity and reduced latency for larger basal dendrites. Cable parameters were: C_m = 1 $\mu F/cm^2$, R_m = 15,000 Ωcm^2, R_a = 150 Ωcm. The apical cylinder is of infinite length with diameter of 3 µm; the basal tree (color cables) have linearly increasing diameter (d) and length (L), approximating the increment from rat to human basal trees (Fig 6F): red (l =800 µm, d = 20 µm), yellow (l = 700 µm, d = 18 µm); green (l = 600 µm, d = 16 µm); light blue (l = 500 µm, d = 14 µm); dark blue (l = 400 µm, d = 12 µm). Soma diameter was 20µm in all cases.

Cell name	C_m ($\mu F/cm^2$)	R_m (Ωcm^2)	R_a (Ωcm)
Human1	0.65	19,875	298
Human2	0.60	15,672	263
Human3	0.85	12,872	103
Human4	0.77	21,523	209
Human5	0.63	15,570	109
Rat1	0.84	13,110	267
Rat2	1.16	9,084	249
Rat3	1.02	14,497	115
Rat4	1.41	8,527	109
Mean human	**0.70**	**17,120**	**196**
Mean rat	**1.11**	**11,304**	**185**

Table 1. Passive cable parameters fitted to experimental data. C_m and R_m are the specific membrane capacitance and resistivity, respectively; R_a is the specific axial resistance.

Cell name	d_{avg} (μm)	l_{avg} (μm)	$L_{avg}(\lambda)$	τ (ms)	Latency (ms)	Velocity (m/s)
Human1	0.4	192	0.6	12.92	2.8	0.074
Human2	0.5	180	0.54	9.46	2.18	0.089
Human3	0.4	172.7	0.42	10.90	2.13	0.086
Human4	0.6	178	0.41	16.60	2.5	0.074
Human5	0.44	162.6	0.35	9.80	1.69	0.098
Rat1	0.35	163.9	0.64	11.00	3.17	0.054
Rat2	0.43	144.3	0.52	10.50	3.52	0.044
Rat3	0.5	170.4	0.32	14.5	3.44	0.051
Rat4	0.53	164.6	0.37	11.9	2.72	0.063
Mean human	**0.47**	**177.1**	**0.46**	**11.9**	**2.26**	**0.085**
Mean rat	**0.45**	**160.8**	**0.46**	**12**	**3.21**	**0.053**

Table 2. Morphological and cable parameters, and model prediction, of the average EPSPs latency and velocity within experimental range of dendritic recordings per modeled cell. Cable parameters were fitted per cell as in Table 1. l_{avg} *and* d_{avg} - the average physical distance and diameter respectively from which the respective experiments (per cell) were performed (zoom-in region in Fig. 7C,D). L_{avg} is the respective distances in cable units ($L = \frac{l}{\lambda}$); τ is the membrane time constant (C_m*R_m). Latency and velocity are the average values from dendrite to soma, computed for the experimental range of dendritic recordings.

Supplementary Materials

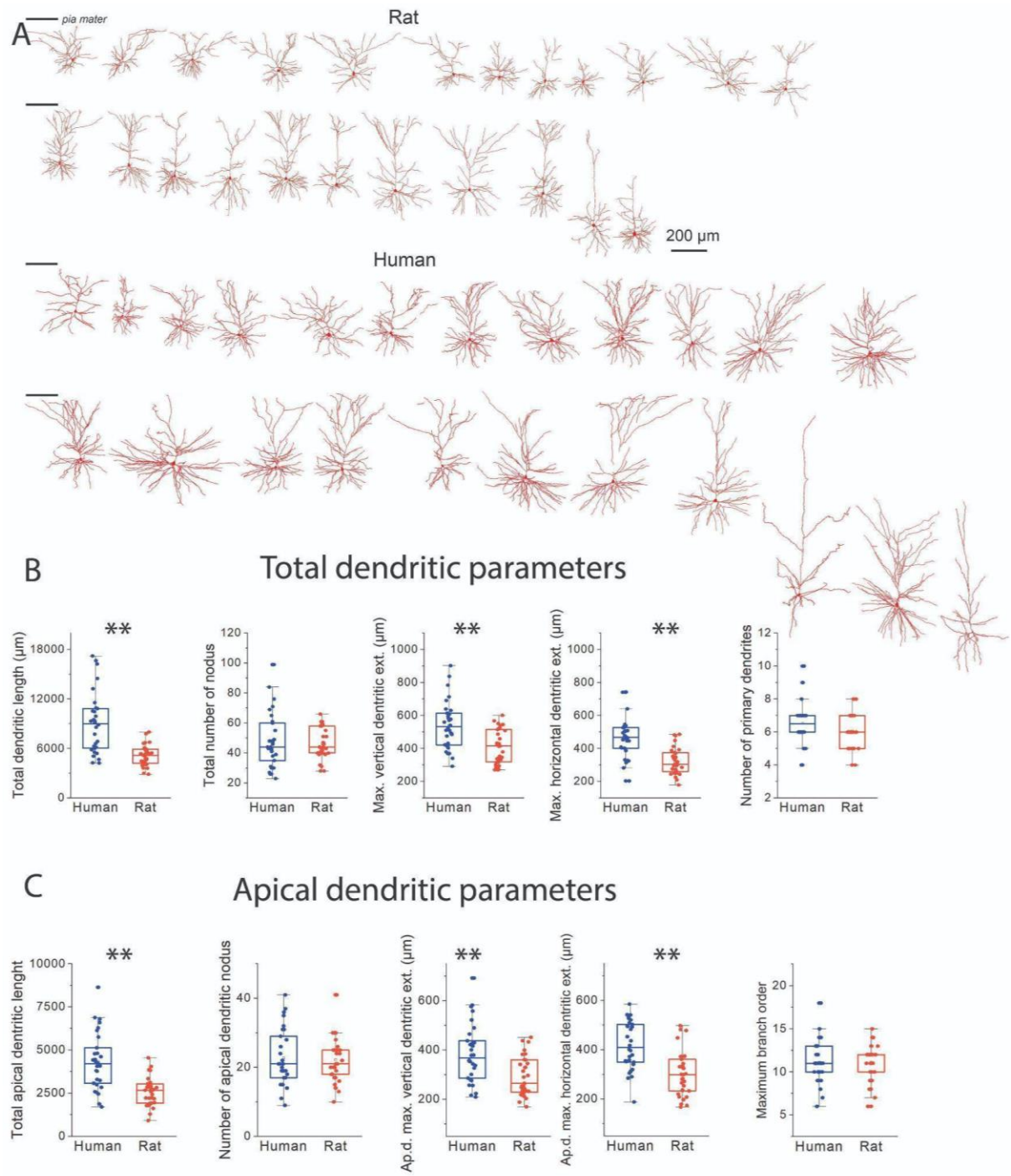

Suppl.Fig. 1. Size comparison of layer 2/3 pyramidal cells in the human and rat cortex. A Sample reconstructions of fully recovered rat and human cortical pyramidal cells. Left horizontal line indicates the location of pia mater. **B** Comparison of dendritic length, number of nodes, maximum vertical and horizontal extension, and the number of primary dendrites respectively of all reconstructed dendritic arborization. **C** Comparison of length, number of nodes, maximum vertical and horizontal extension and the number of maximum branch order respectively of the apical dendrites. Boxes represent median and IQR, whiskers represent outlier range (±1.5 IQR); mean is indicated by open square, crosses denote minimum and maximum values. ** denotes significant difference $P < 0.01$.

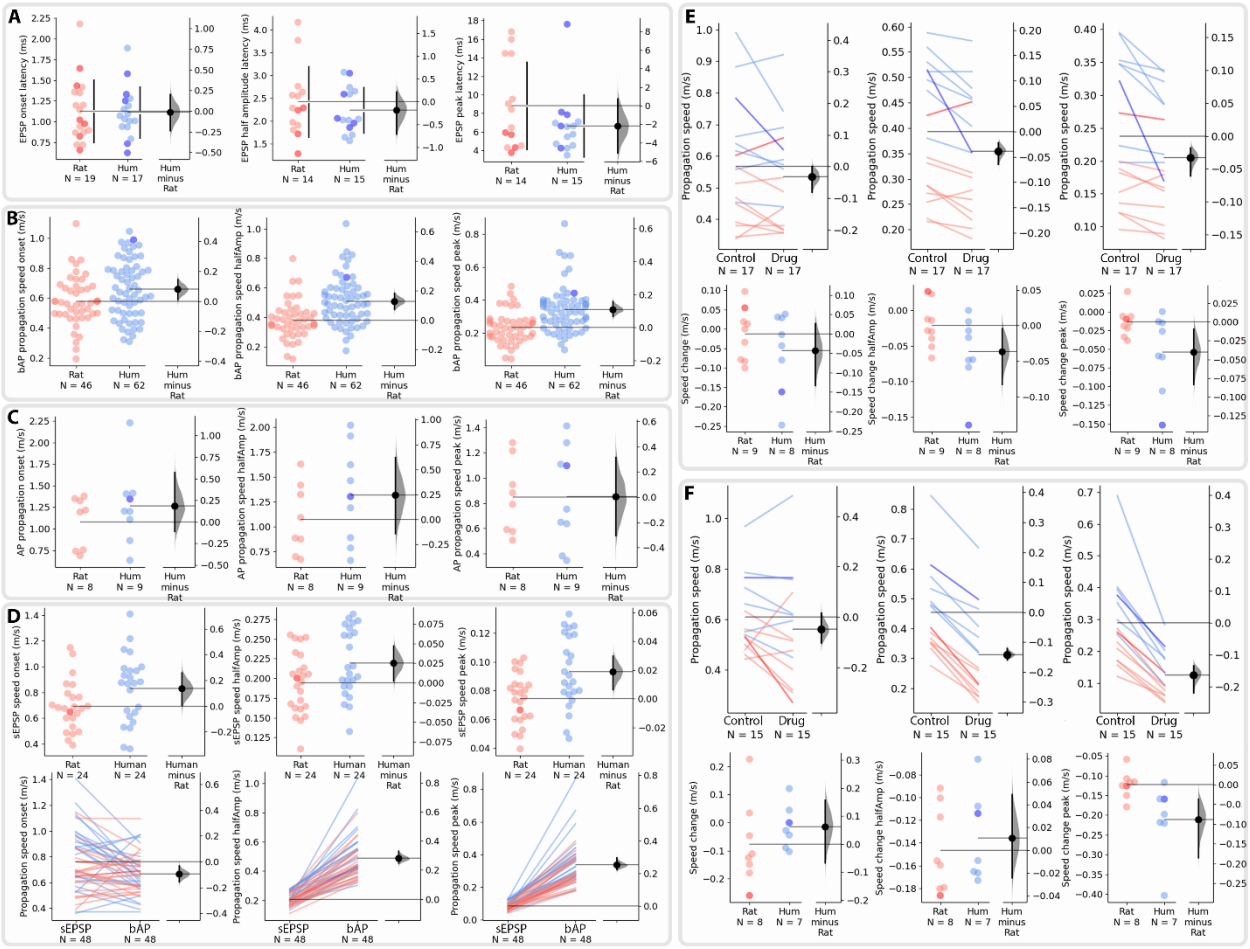

Suppl.Fig.2 Latencies and propagation speed measured at different points of the propagating waveforms. A The presynaptic AP peak and EPSP latency were measured at different points. Left: latency at onset, middle: latency at half amplitude, right: latency at EPSP peak. **B** Same as A but for bAP speed values. **C** Same as A but for AP axonal speed values. **D** Upper: Same as A but for sEPSP speed values. Lower: comparison of sEPSP and bAP speed. **E** Pharmacological experiments with ZD7288. **F** Same as E but for a cocktail of TTX, $CdCl_2$, and AP5.

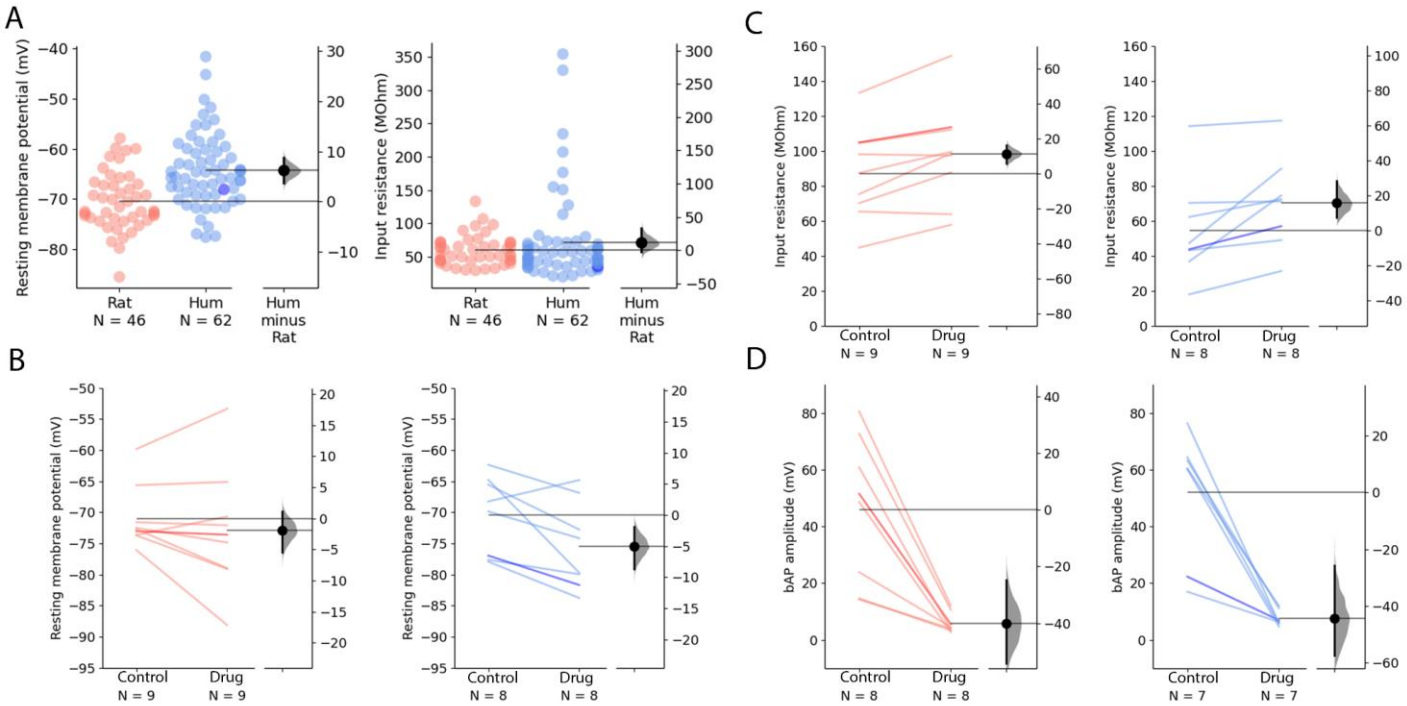

Suppl.Fig.3. Properties of dendro-somatic recording and measured membrane parameters.
A Resting membrane potential of the recorded cells (rat: -70.49 ± 5.78 mV, human: -64.30 ± 7.28 mV, Mann-Whitney U test: P = 7.37× 10^{-6}) were different in human and in rat pyramidal cells. Input resistance of recorded cells (rat: 59.56 ± 21.86 MΩ, human: 71.37 ± 65.48 MΩ, Mann-Whitney U test: P = 0.3466). **B** Resting membrane potential of recorded cells after ZD7288 application (red, rat control: -70.98 ± 5.04 mV vs rat ZD7288: -72.88 ± 9.75 mV, Wilcoxon signed ranks test: P = 0.40694; blue, human control: -70.43 ± 6.28 mV vs human ZD7288: -75.47 ± 6.991 mV, paired sample t test: P = 0.02682). **C** The input resistance changed significantly in rat (red, rat control: 86.95 ± 26.34 MΩ vs rat ZD7288: 98.18 ± 28.53 MΩ, paired sample t test: P = 0.00488) and human (blue, human control: 54.38 ± 28.8 MΩ vs human ZD7288: 70.21 ± 26.09 MΩ, paired sample t test: P = 0.02434) after the application of 20 µM ZD7288. **D** Effect of voltage gated ion channel blockage on bAP amplitude. The amplitudes of the bAPs were significantly decreased upon the application of voltage gated ion channel blockers (rat control: 46.32 ± 25.78 mV vs rat TTX, $CdCl_2$, AP5: 6.26 ± 3.47 mV, paired sample t test: P = 0.00188, human control: 51.95 ± 22.81 mV vs. human TTX, $CdCl_2$, AP5: 7.52 ± 2.84 mV, Wilcoxon signed ranks test: P = 0.0156).

Cell name	Length factor	Diameter factor
Human1	1.26	0.84
Human2	1.03	1.00
Human3	1.24	0.95
Human4	1.25	1.23
Human5	1.26	0.99
Rat1	1.05	1.12
Rat2	1.45	1.11
Rat3	1.67	1.33
Rat4	1.08	1.37

Suppl. Table 1. Morphological scaling factors due to fixation.

Cell name	l_{avg} (μm)	L_{avg}	Latency (ms)	Velocity (m/s)
Human1	192	0.45	2.52	0.08
Human2	180	0.38	2.49	0.08
Human3	172.7	0.43	2.67	0.07
Human4	178	0.38	2.31	0.08
Human5	162.6	0.38	2.24	0.08
Rat1	163.9	0.45	3.1	0.05
Rat2	144.3	0.32	3.44	0.04
Rat3	170.4	0.36	3.65	0.05
Rat4	164.6	0.33	3.1	0.06
Mean human	**177.1**	**0.40**	**2.45**	**0.08**
Mean rat	**160.8**	**0.37**	**3.32**	**0.05**

Suppl. Table 2. Model prediction of the average EPSPs latency within experimental recording distance range per modeled cell for the case of identical cable parameters for all cells. l_{avg} is the average physical distance from which the respective experiments (per cell) were performed (zoom-in region in Fig. 6A,B). d_{avg} is the average diameter at the same range. L_{avg} is the respective distances in cable units ($L = \frac{l}{\lambda}$). Latency is the average latency measured at the experimental distance. Uniform cable parameters were used for all cells as in Figure 6.

Cell name	l_{avg} (μm)	L_{avg}	Latency (ms)	Velocity (m/s)
Human1	192	0.45	3.86	0.05
Human2	180	0.38	2.89	0.07
Human3	172.7	0.43	3.94	0.05
Human4	178	0.38	3.32	0.06
Human5	162.6	0.38	3.1	0.05
Rat1	163.9	0.45	3.4	0.05
Rat2	144.3	0.32	3.1	0.05
Rat3	170.4	0.36	3.2	0.06
Rat4	164.6	0.33	3.1	0.06
Mean human	**177.1**	**0.40**	**3.42**	**0.056**
Mean rat	**160.8**	**0.37**	**3.2**	**0.053**

Suppl. Table 3. Model prediction of the average EPSPs latency within experimental recording distance range per modeled cell for the case of identical cable parameters and "hybrid cell" whereby all modeled cells consist of the basal tree of "Rat4". l_{avg} is the average physical distance from which the respective experiments (per cell)

were performed (zoom-in region in Fig. 6E,F). d_{avg} is the average diameter at the same range. L_{avg} is the respective distances in cable units ($L = \frac{l}{\lambda}$). Latency is the average latency measured at the experimental distance. Uniform cable parameters were used for all cells as in Figure 6.

Cell name	l_{avg} (μm)	L_{avg}	Latency (ms)	Velocity (m/s)
Human1	192	0.6	3.8	0.06
Human2	180	0.54	2.5	0.08
Human3	172.7	0.42	3.03	0.06
Human4	178	0.41	3.5	0.06
Human5	162.6	0.35	2.29	0.07
Rat1	163.9	0.64	3.33	0.05
Rat2	144.3	0.52	3.26	0.045
Rat3	170.4	0.32	3.02	0.06
Rat4	164.6	0.37	2.69	0.06
Mean human	**177.1**	**0.46**	**3.0**	**0.056**
Mean rat	**160.8**	**0.46**	**3.1**	**0.053**

Suppl. Table 4. Model prediction of the average EPSPs latency within experimental recording distance range per modeled cell for the case of fitted cable parameters per cell and "hybrid cell" where all modeled cells consist of "Rat4" basal tree. l_{max} is the maximal physical distance from which the respective experiments (per cell) were performed (zoom-in region in Fig. S8 A,B). d_{max} is the (average) diameter at l_{max}. L_{max} is the respective distances in cable units ($L = \frac{l}{\lambda}$); τ is the membrane time constant (C_m*R_m). Latency is the average latency measured at the maximal distance. Fitted cable parameters were used for all cells as in Figure 7.

Factor affecting EPSP latency	Coefficient	Std. Error	z-value	p-value	95% Confidence Interval
Intercept	0.6698	0.009	77.910	<0.001	[0.653, 0.687]
1. **distance** of synapse from soma (z-score)	-0.2833	0.005	-61.165	<0.001	[-0.292, -0.274]
2. **species** (human vs. rat as reference)	0.0770	0.007	10.694	<0.001	[0.063, 0.091]
3. "**hybrid** cell" manipulation (compared to original cells)	-0.0751	0.007	-10.470	<0.001	[-0.089, -0.061]
4. **radius** (z-score)	0.0300	0.005	6.651	<0.001	[0.021, 0.039]
5. "**Fitted**": Specific cable parameters (cell-based fitting vs. uniform parameters as reference	0.0298	0.007	4.233	<0.001	[0.016, 0.044]

Suppl. Table 5. Examining factors influencing EPSP latency via GLM model without interaction terms. Note the ranking (1-5) of the factors affecting EPSP latency (in ms units). Factors were ranked (1-5) based on the magnitude of their absolute coefficients, which provide insight into their relative contribution to the model. The model was fit using the Gamma family and included continuous factors that were standardized prior to fitting, as well as categorical factors (see comments above for the reference values). Each factor used in the model's formula is highlighted in bold. The formula used for the model: latency ~ species + distance + hybrid + radius + fitted.

Factor affecting EPSP latency and their interactions	Coefficient	Std. Error	z-value	p-value	95% Confidence Interval
Intercept	0.5998	0.007	81.071	<0.001	[0.585, 0.614]
distance of synapse from soma (z-score)	-0.2379	0.010	-23.228	<0.001	[-0.258, -0.218]
species (human vs. rat as reference)	0.1640	0.010	15.752	<0.001	[0.144, 0.184]
radius (z-score)	-0.0049	0.006	-0.799	0.424	[-0.017, 0.007]
radius × species (human)	0.0755	0.009	8.301	<0.001	[0.058, 0.093]
distance × species (human)	-0.0690	0.013	-5.151	<0.001	[-0.095, -0.043]
distance × species (rat) × hybrid (True)	-0.0007	0.011	-0.065	0.948	[-0.022, 0.020]
distance × species (human) × hybrid (True)	-0.0510	0.008	-6.512	<0.001	[-0.066, -0.036]
distance × species (rat) × fitted (True)	-0.0040	0.011	-0.377	0.706	[-0.025, 0.017]
distance × species (human) × fitted (True)	0.0233	0.008	3.031	0.002	[0.008, 0.038]

Suppl. Table 6. Examining factors influencing EPSP latency via GLM model with interaction terms. This table presents evidence of significant interactions between the main factors affecting EPSP latency (see Suppl. Table 5 for the non-interaction model). The model was fit using the Gamma family and included continuous factors that were standardized prior to fitting, as well as categorical factors (see Supp. Table 5 for the reference value). The formula used for the model (names match the factors from Suppl. Table 5): latency ~ species + distance + radius + (species×fitted×distance) + (species×hybrid×distance) + (species×radius).

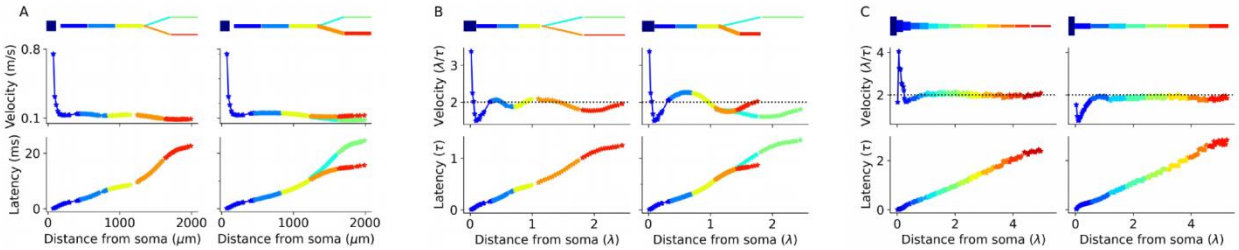

Suppl.Fig.4. Morphological irregularities affect EPSP latency and velocity. A Cable with a single branch, with symmetrical (top left) or asymmetrical (top right) branches. Thick branches diameter is 4μm, while thin branches' diameter is 1μm. Latency and velocity were calculated as explained in the text and in Figs. 7 and 8; synaptic inputs were activated at different sites along the structure. The recording site ("soma") is at left (dark blue rectangle), with diameter of 13μm. **B** As in A, with normalized space and time constants. For symmetrical branches, both latency and velocity overlap for the two branches (left column in both **A** and **B**), while in asymmetrical case, the latency from the thick branch is smaller as it is electrotonically closer to the soma and, therefore, for the same physical distance the initial velocity of the EPSP at its site of origin is larger (right column in **B**, red branch compared with green). However, there is a small increase in latency (decrease in velocity at these daughter branches) due to local impedance mismatch. **C**. Cable with diameters replicating the apical main-branch of 'Human2' (left column) and 'Rat1' (right column) PCs. Note the local irregularities shifts the velocity above (left column) or below (right column) $2\lambda/\tau$ despite having identical lengths across all sections. Moreover, velocity pattern changes due to the proximity of the synapse to the soma, as a function of the cable diameters. Cable parameters are identical for all morphologies (C_m = 1.5 $\mu F/cm^2$, R_m = 10,000 Ωcm^2, R_a = 150 Ωcm).

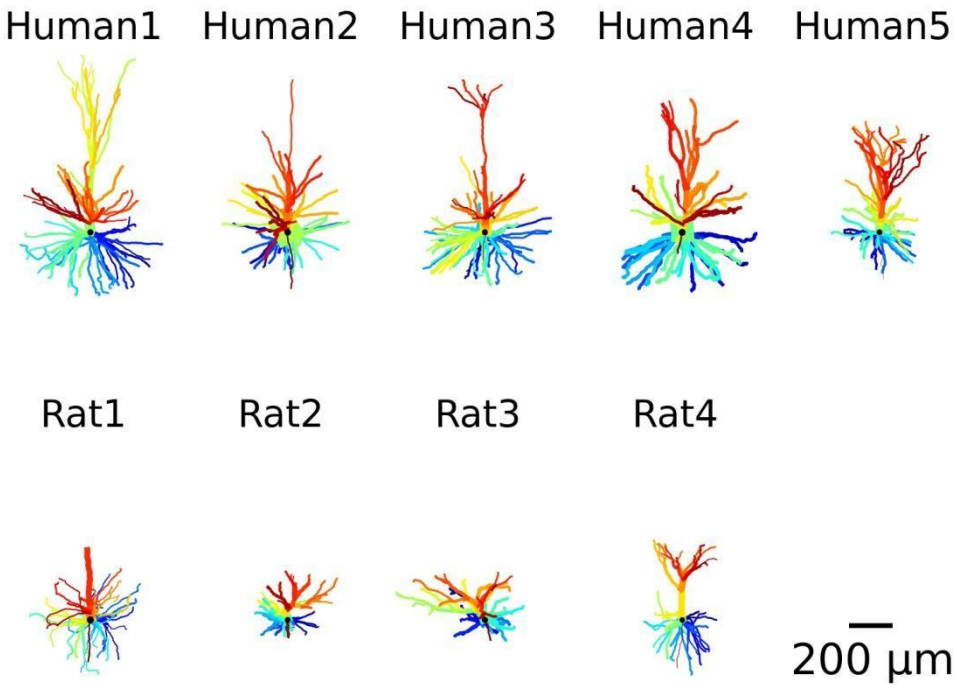

Suppl.Fig.5. Morphology of the nine modeled cells. Each dendritic branch is marked by a different color.

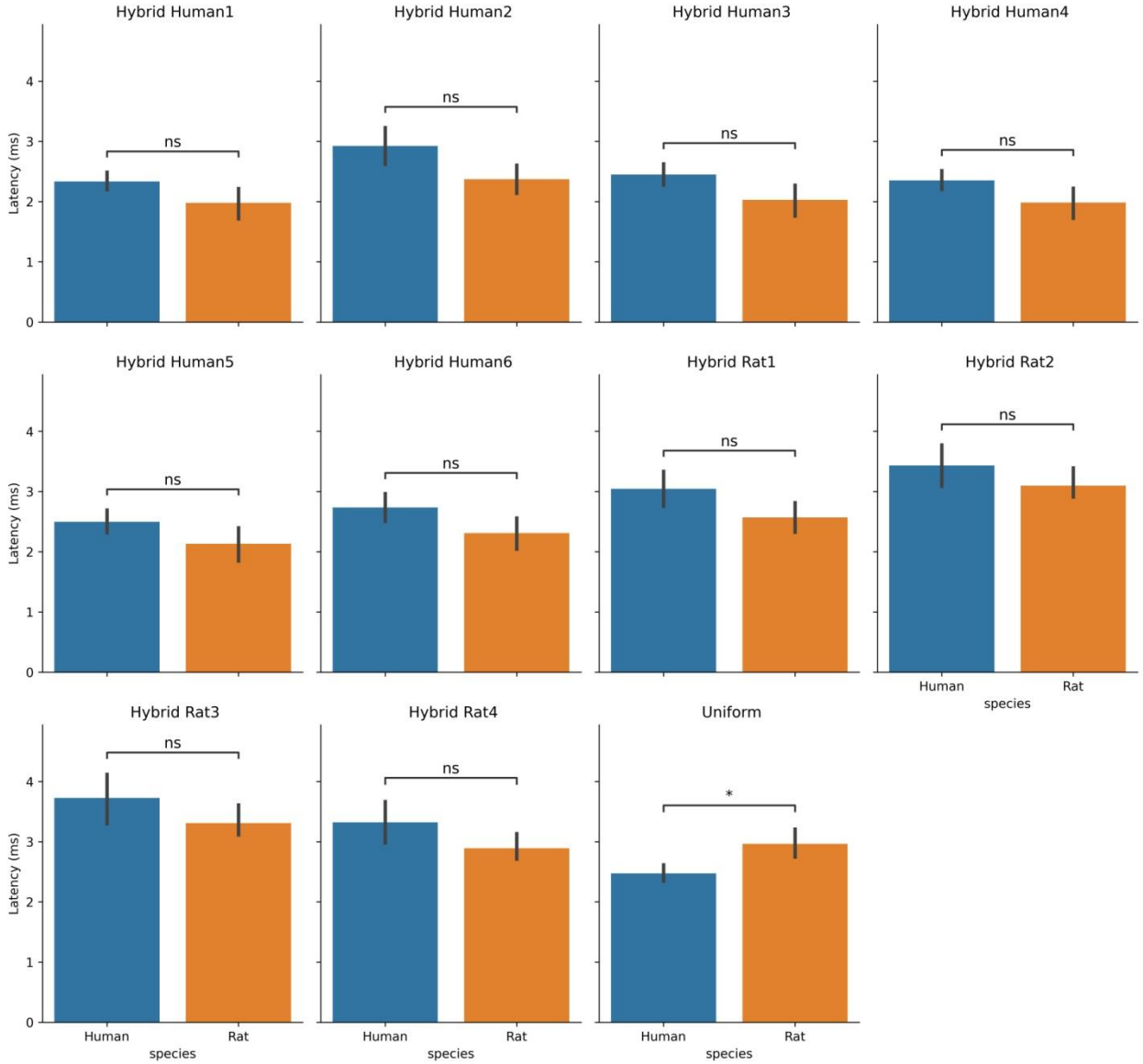

Suppl.Fig.6. Quantifying the effect of switching the basal tree between rat and human (and vice versa- the 'hybrid cells' on mean latency, uniform parameters. Average latency as a result of using each of the nine modeled cells basal trees as the basal tree of all other cells (e.g. a "hybrid cell"), compared with original models latencies (e.g. "Uniform"). Average latency was calculated similar to Suppl. Table 2-4 Note the acceleration due to most of the human basal trees versus the deceleration due to rat basal trees. Mann-Whitney U test. * denotes significant difference $P < 0.05$.

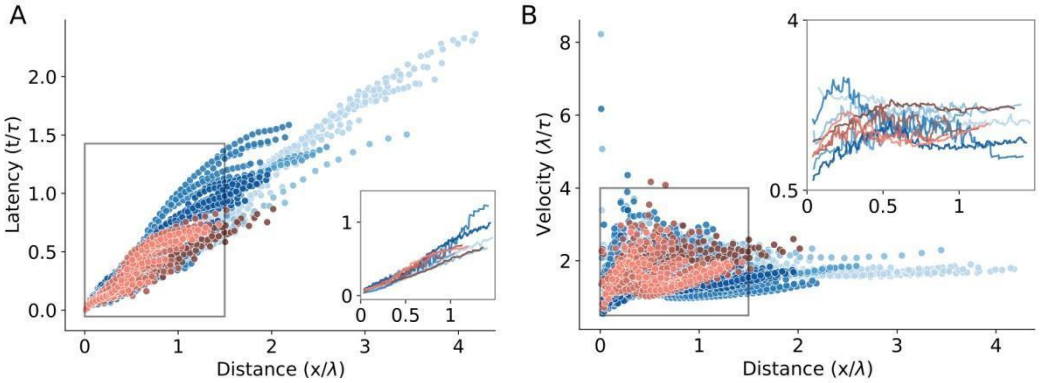

Suppl.Fig.7. 'hybrid cells' effect on latency and velocity for the experimentally-fitted cable parameters. A,B Same as Fig 7E,F but for 'hybrid cells', computed for the 5 human neurons, all having the basal tree of 'Rat4' (in blue) and for the 4 rat cells, all with the basal tree of 'Rat1' (in red). Note that the differences in latency and velocity between human and rat were diminished (insets).

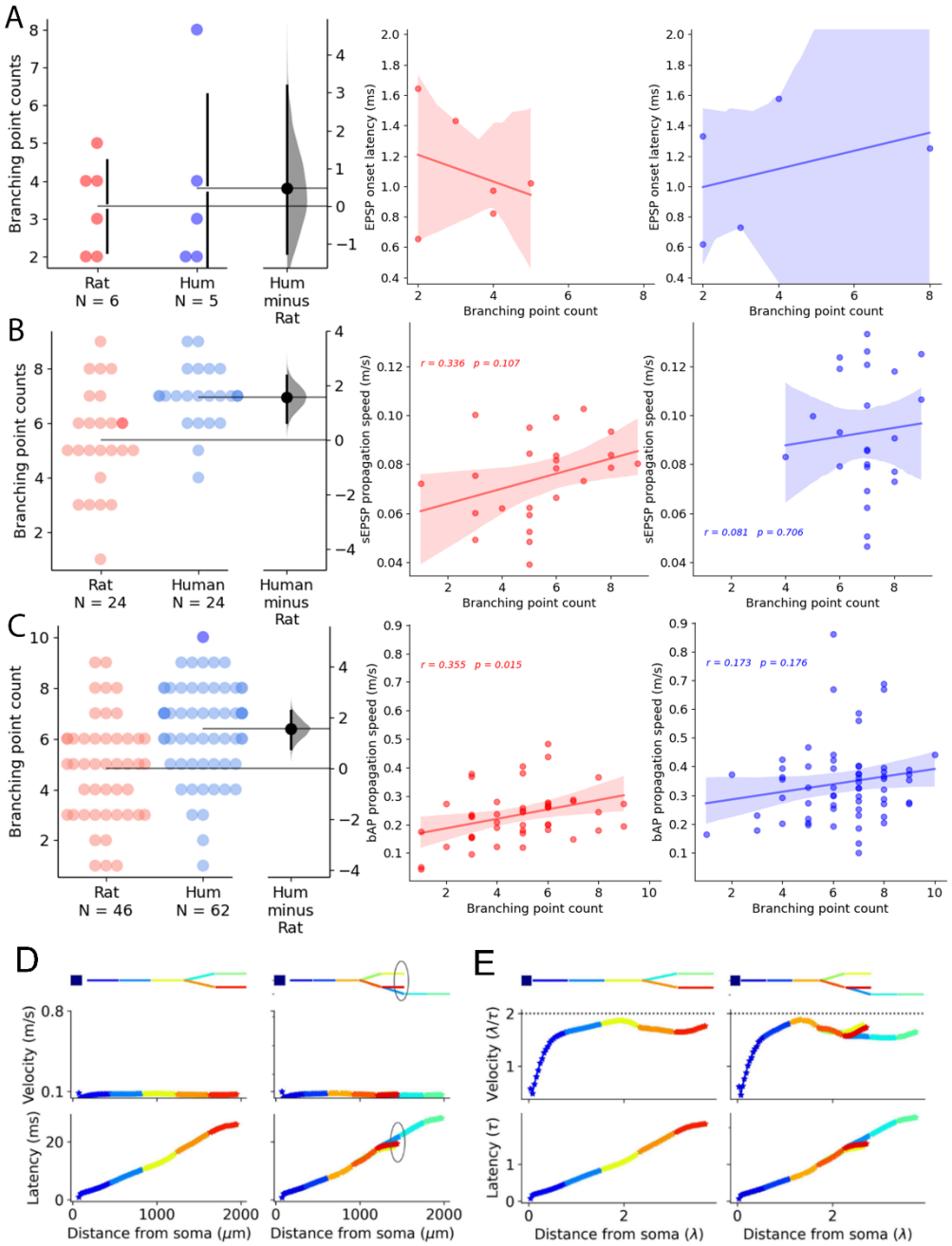

Suppl.Fig.8. Effect of dendritic branching points on signal propagation velocity. **A** Dendritic branching point counts between the putative synapse and the soma of the postsynaptic cells of the fully reconstructed cell pairs. We could not find significant correlation between synaptic latency and branching point counts (Red: rat, Blue: human). **B** Branching point counts between the dendritic recording site and the soma during sEPSP recordings. We could not find significant correlation between branching point count and sEPSP propagation speed. **C** Branching point counts between the dendritic recording site and the soma during bAP recordings. We found a significant correlation between branching point count and bAP propagation speed in the rat dataset (red) but not in the human dataset (blue). **D** Simulation of the effect of a branching point on the signal propagation velocity. Adding a branch point (yellow versus red, marked with a circle) to the dendrite did not affect the velocity and the latency of the simulated signal. **E** Same as D but for cable units.

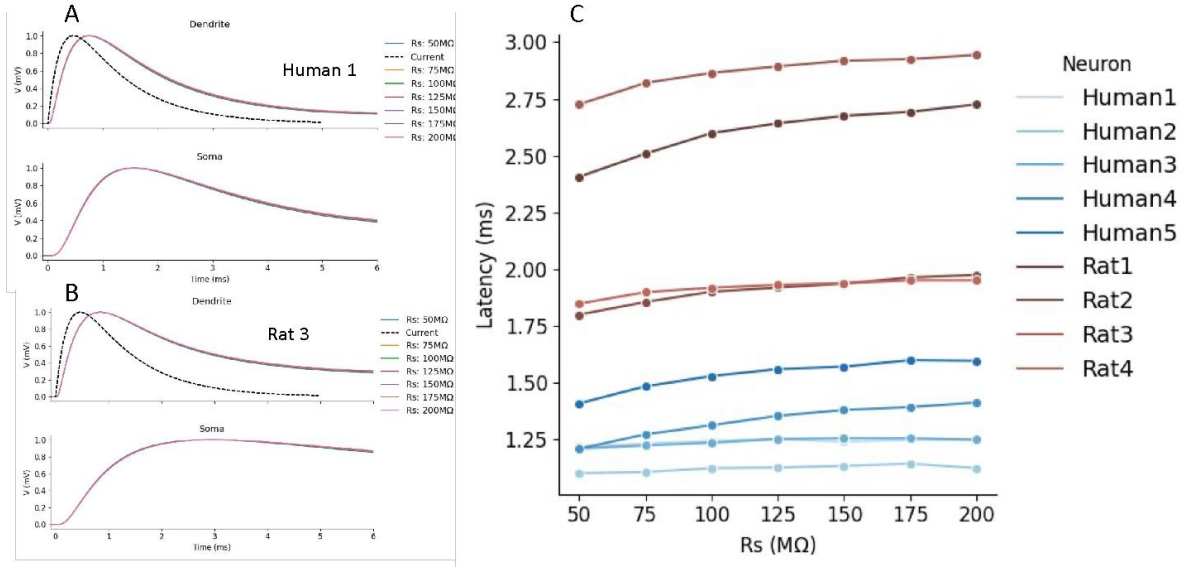

Suppl.Fig.9. Effect of series resistance of the dendritic electrode on measurement of EPSP latency. A. Top: simulated EPSPs in Human 1 neuron as recorded at the injected point in the apical dendrite, located 150 µm from the soma. Simulated synaptic current is shown by the dashed line. Bottom: the resultant EPSP at the soma. Simulation was performed for a range of series resistance (Rs) values (shown at right). B. As in A but for Rat 3 neuron. C. EPSPs latency as a function of Rs for the 9 modeled neurons. Electrode capacitance was 6pF with variable series resistance, Rs.

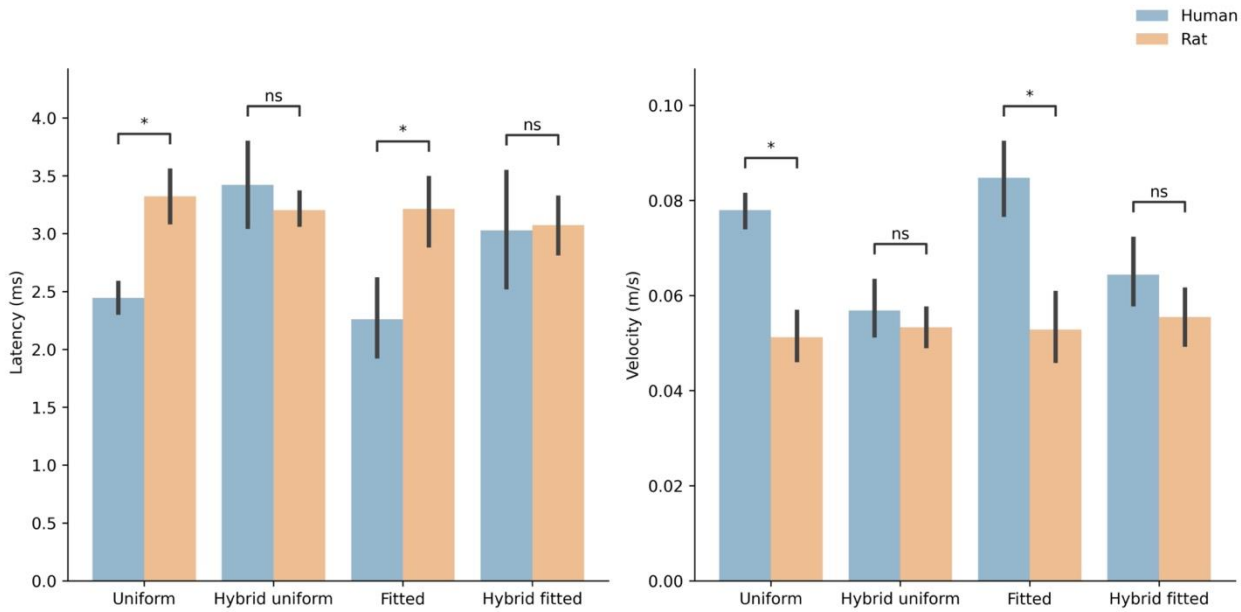

Suppl.Fig.10. 'Hybrid cells' effect on latency and velocity for the experimentally-uniform vs fitted cable parameters. Values as in Table 2 and Suppl.Tables 2-4. Note that the differences in latency and velocity between human and rat are significant in fitted and uniform parameters and diminished in "Hybrid" case. * denotes significant difference $P < 0.05$. Mann-Whitney test, with Bonferroni correction.

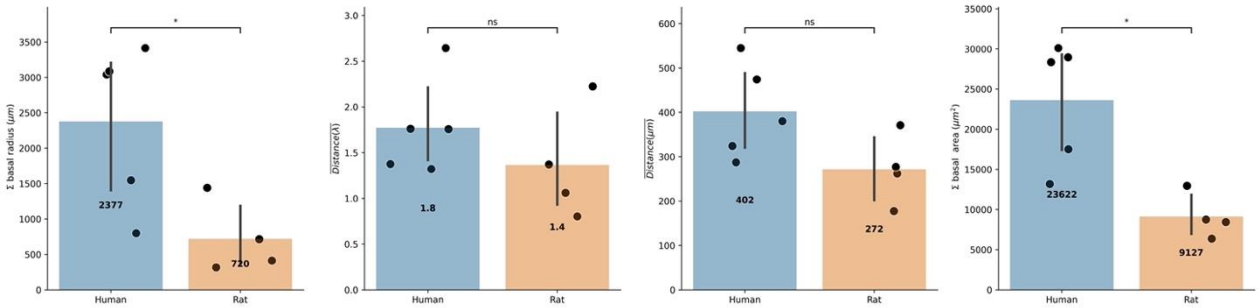

Suppl.Fig.11. Basal load effect. Significant difference between human and rat's basal load, despite no significant difference in real and cable distance of basal tree.

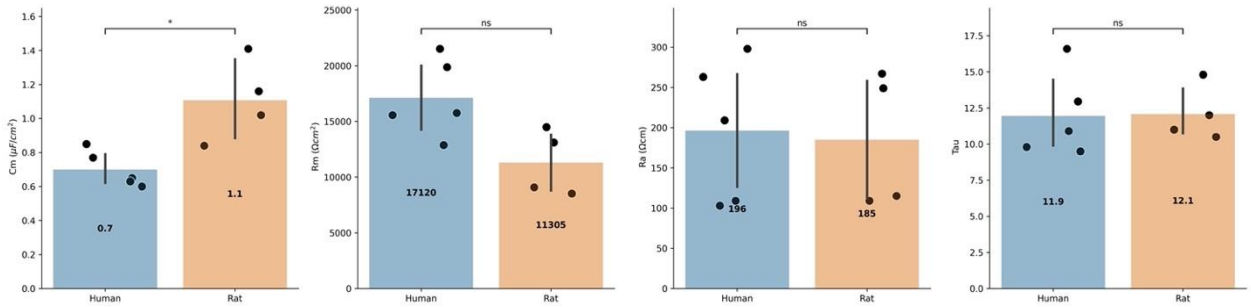

Suppl.Fig.12. Passive cable parameters fitted to experimental data. C_m and R_m are the specific membrane capacitance and resistivity, respectively; R_a is the specific axial resistance. Note the similar time-constant between human and rat.

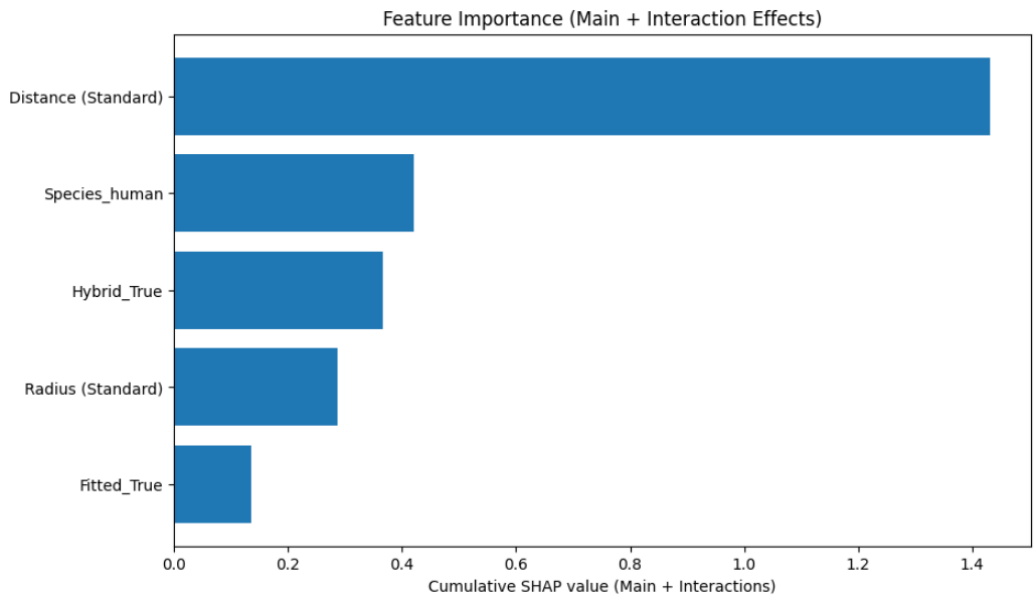

Suppl.Fig.13. SHAP analysis feature importance result. Cumulative SHAP values (main and interaction effects) for the top five variables influencing signal propagation latency. The model used for this analysis is the Gradient Tree Boosting model.